Mechanical properties and recrystallization of quartz in presence of H_2O: combination of cracking, subgrain rotation and dissolution-precipitation processes

*Petar Pongrac [a, *], Petr Jeřábek [a], Holger Stünitz [b, c], Hugues Raimbourg [c], Renée Heilbronner [b, d], Martin Racek [a] and Lucille Nègre [c]*

[a] Institute of Petrology and Structural Geology, Faculty of Science, Charles University in Prague, Albertov 6, 128 43, Praha 2, Czech Republic.

[b] Department of Geosciences, Arctic University of Norway, PO Box 6050 Langnes, 9037 Tromsø, Norway.

[c] Institute of Earth Sciences, University of Orléans, 1A Rue de la Ferollerie, 45071 Orleans Cedex 2, France.

[d] Department of Environmental Sciences, University of Basel, Bernoullistrasse 32, 4056 Basel, Switzerland.

*Corresponding author: Faculty of Science, Charles University, Albertov 6, 128 43, Praha 2, Czech Republic; tel: +385996742123

e-mail addresses: pongracp@natur.cuni.cz (P. Pongrac), jerabek.petr@natur.cuni.cz (P. Jeřábek), holger.stunitz@uit.no (H. Stünitz), hugues.raimbourg@univ-orleans.fr (H. Raimbourg), renee.heilbronner@unibas.ch (R. Heilbronner), martin.racek@natur.cuni.cz (M. Racek), lucille.negre@univ-orleans.fr (L. Nègre)

KEYWORDS: quartz, deformation experiments, H_2O, recrystallization

HIGHLIGHTS:

- Recrystallization of quartz in the presence of H_2O in our experiments occurs by subgrain rotation, cracking and dissolution-precipitation processes
- H_2O-promoted grain boundary migration causes reconstitution of quartz, reflected by blue luminescence
- Sample strength is controlled by crystal plasticity of original quartz grains with no significant contribution from cracking
- Slightly lower strength of H_2O-added samples and low stress exponent values (~2) are explained by enhanced dissolution-precipitation and grain boundary sliding operating together with dislocation creep
- Recrystallization accompanying cracking is more pronounced in the H_2O-added samples

Abstract

Natural quartzite samples, as-is and with 0.1 wt% of added H_2O, have been deformed up to ~30% bulk strain in axial shortening experiments with constant strain rate of ~10^{-6} s^{-1} at 900 °C and 1 GPa, and in strain rate stepping ~10^{-5} to ~10^{-7} s^{-1} at 900 °C and 1-1.5 GPa, in order to investigate the role of H_2O in deformation and recrystallization of quartz. H_2O-added samples showed ~30 MPa lower mean strengths than as-is samples. Samples weaken slightly after 15% strain with mean flow stresses in the range of 154-227 MPa, and stress exponent (*n*) values between 1.45 and 2.13. The original quartz grains have been deformed plastically (dislocation glide). Discrete mode I cracks without detectable offset have developed in addition to plastic strain. Deformation was associated with recrystallization of up to 20% of the material in the most deformed parts of the samples. New grains were nucleated by both cracking and subgrain rotation, and were largely reconstituted by H_2O-promoted grain boundary migration, related to dissolution-precipitation processes. This reconstitution of material is documented by a change in luminescence to blue, caused by trace elements exchange in quartz structure. The blue luminescence is prominent along healed cracks and high angle grain boundaries while it was not observed along the low angle boundaries formed by subgrain rotation. Compared to the as-is samples, the crack-related recrystallization is more frequent in the H_2O-added samples. The low stress exponent values may indicate dissolution-precipitation and grain boundary sliding processes to accommodate incompatibilities at grain boundaries arising from an insufficient number of active slip systems. We suggest that the ubiquitous presence of H_2O in nature may promote recrystallization of quartz by combinations of cracking, dislocation glide and creep and dissolution-precipitation processes.

1. Introduction

Quartz, among other rock forming minerals, is a ubiquitous constituent in rocks of the continental crust. It usually represents one of the mechanically weakest phases at temperatures above the brittle to plastic transition, so that its rheology has a major impact on the strength of continental crust (Brace and Kohlstedt, 1980; Kohlstedt et al., 1995). Since the pioneering experiments by Griggs and Blacic (1965), it is well-known that the strength of quartz decreases substantially in the presence of H_2O (e.g., Griggs, 1967; Blacic, 1975; Blacic and Christie, 1984; Kronenberg and Tullis, 1984; McLaren et al., 1989; FitzGerald et al., 1991; Doukhan, 1995; Kohlstedt et al., 1995; Stipp et al., 2006; Stünitz et al., 2017; Tokle et al., 2019). However, a comprehensive and validated microphysical model behind this phenomenon is still incomplete or missing.

The original concept of hydrolyzed Si-O bonds (Griggs 1967, 1974) lowering the Peierls stress for dislocation glide ("hydrolytic weakening"), had been challenged by the extremely low potential of the quartz crystal structure to incorporate molecular H_2O or its dissociated forms (Kronenberg et al., 1986; Rovetta et al., 1986; Paterson 1986; Gerretsen et al., 1989). Instead, entrapment of H_2O in the form of fluid inclusions or molecular clusters (Kekulawala et al., 2013; Paterson, 1986; McLaren et al. 1989; Tarantola et al., 2010) is common in synthetic and natural quartz. During deformation, such H_2O may be redistributed by microcracking and crack-healing (Kronenberg et al., 1986; Gerretsen et al., 1989; FitzGerald et al. 1991; Trepmann and Stöckhert, 2003; Tarantola et al., 2010;

Stünitz et al., 2017) or by the movement of dislocations (Bakker and Jansen 1990; Cordier et al. 1994; Stünitz et al., 2017). In this case, the weakening effect has been attributed to generation and multiplication of dislocations in the vicinity of such H_2O-inclusions or -clusters (Morrison-Smith et al., 1976; McLaren et al., 1989; FitzGerald et al., 1991; Stünitz et al., 2017) and/or by hydration of dislocation cores, facilitating their glide (Paterson, 1989; Stipp et al., 2006, Tarantola et al., 2010). Alternatively, cracking and crack healing of natural quartz samples during an early stage of deformation experiments may also generate glissile dislocations. Crystal plasticity in the vicinity of healed cracks may be facilitated in crystals that otherwise are devoid of dislocations or show low dislocation density (Fitz Gerald et al. 1991; Stünitz et al. 2017).

In addition to the glide of dislocations, enhanced crystal plasticity and deformation to large strains requires the recrystallization and/or recovery of material with high dislocation densities to counteract the hardening effect of pinning dislocations (e.g., McLaren and Retchford, 1969). Recrystallization at high temperatures is achieved by two principal processes: grain boundary migration (GBM; e.g., Poirier and Guillopé, 1979; Hirth and Tulis, 1992) and by the formation of subgrain boundaries and progressive rotation of subgrains to nucleate new grains (SGR; e.g., Dell'Angelo and Tullis, 1989, Gleason et al., 1993; Stipp et al., 2002a). The GBM process leads to reconstitution (re-creation) of the crystal structure, which in the presence of H_2O may take place by dissolution and precipitation of material across a grain boundary (e.g., Guillopé and Poirier, 1980; Stipp and Kunze, 2008). In this contribution, we include the dissolution-precipitation in the GBM process, because the distinction between fluid-absent and fluid-present GBM in nature appears to be very difficult or impossible. The availability of H_2O at grain boundaries appears to promote the rate of the GBM by dissolution-precipitation processes and contributes favorably to the reconstitution of quartz during crystal plastic deformation (e.g., Urai et al., 1986; Drury and Urai, 1990).

The interaction of several processes resulting in nucleation of new grains, especially at a small local scale in the vicinity of grain boundaries, is often termed "bulging recrystallization" (Bailey and Hirsch, 1962; Stipp et al., 2002a,b). Despite the development of some more precise models describing nucleation processes (e.g., Stipp et al., 2002a; 2006), the mechanisms of the nucleation of new grains are still poorly understood. SGR is considered to be the most important nucleation process, but cracking has also been observed and inferred as a mechanism for nucleating new grains (den Brok and Spiers, 1991; Stünitz et al., 2003; Vernooij et al., 2006; Trepmann and Stöckhert, 2013). After the new grains are formed by cracking and fragmentation, the grain boundaries may be sufficiently mobile to migrate and produce rounded grain shapes, so that the crack-related origin of the new grains can be difficult to detect. Dilatancy as a consequence of cracking may contribute to precipitate material during a GBM process (e.g., Précigout and Stünitz, 2016).

The aim of the present study is to decipher the recovery processes in quartz material during deformation in the presence of an aqueous fluid. In addition, a process for the nucleation and production of new grains during recrystallization of quartz is inferred. Implications for the effect of H_2O on crystal plastic deformation are discussed.

2. Experiments and analytical methods

The starting material used for experiments in this study is a late Precambrian quartzite from the Austertana region (ELKEM quarry) in northern Norway (see description in Nègre et al., 2021). The material is known for its low content of accessory phases such as phyllosilicates or Fe-oxides and hydroxides (Pevik, 2015). Because of its purity, the material has been widely used for industrial and technical purposes.

The quarry is positioned at the top part of the Gamasfjell formation, which extends over more than 300 km^2 and shows a thickness of up to 300 m (Størseth and Wanwik, 1992). The formation is interpreted as part of a Precambrian shallow marine sedimentary complex deposited in tidal and subtidal environments (Johnson et al., 1978). No traces of subsequent deformation or metamorphism have been identified in the sampled material.

2.1. Sample preparation

Cylindrical cores were drilled from unoriented rock samples, with a size of 6.35-6.55 mm in diameter and 13-14 mm in length. The top and bottom cylinder planes were ground plane-parallel and normal to the cylinder axis. All sample cylinders were pre-dried in an oven at ~115 °C for at least 24 hours. After they cooled down, they were wrapped in nickel foil and inserted into pre-annealed platinum jackets. Part of the samples was encapsulated as-is after drying, while in others, 0.1 wt% of distilled H_2O was added prior to encapsulation. In the following text, samples are accordingly referred to as "as-is" and "H_2O-added" samples, respectively. All jackets were weld-sealed using a millisecond-pulsed Lampert PUK 3 professional plus welding system, which caused negligible loss of added H_2O during the welding process.

Alumina pistons with a diameter of ~6.33 mm were used in the sample pressing assembly, touching the Pt-capsule with the sample. NaCl was used as a confining medium. A graphite resistance furnace, supported by inner and outer pyrophyllite sleeves, was used to heat the assembly. S-type thermocouples (Pt and Pt-Rh wires) positioned at ~30% of the sample length were used for temperature control (**App. 1**). The temperature difference between the measuring point and the upper alumina piston was estimated to be up to 10% (Pec et al., 2016). A tungsten carbide plug was used as a bottom base of the assembly, while the contact between σ_1 and σ_3 steel pistons and the assembly is maintained by a ~7.5 mm thick lead seal. The entire sample assembly is schematically presented in **Appendix 1**, and more detailed description can be found in Pec et al. (2012).

2.2. Deformation experiments

Deformation experiments were performed at the Department of Geosciences, University of Tromsø, using the Griggs-type solid-medium apparatus (Griggs, 1967; Tullis and Tullis, 1986). All experiments have been carried out in axial shortening setup (**App. 1**) at controlled predefined temperature, confining pressure and strain rate. An example of a mechanical record of an experiment with described technical details is presented in **Appendix 2**.

Force applied to the σ_1 piston was measured by an external load cell. Displacement of the σ_1 piston was recorded using a direct current transducer with resolution of ~1 μm. Together with the confining pressure measured as oil pressure in the hydraulic ram, all data were digitally recorded at a frequency of 1 Hz. Values of the maximum principal stress were derived from the applied force

(kN), using corrections for increasing sample cross sectional area and fluctuations of confining pressure. Differential stress was calculated as $\Delta\sigma = \sigma_1 - \sigma_3$ with both minimum and maximum principal stress calibrated with respect to the confining pressure at the hit-point. Determination of the hit-points is explained in more detail in **Appendix 2**. For the construction of the strain vs. stress curves of the strain rate stepping experiments, the original hit-point was used for all steps. The sensitivity of the external load cell allows for determination of the differential stress within an error of +/- 30 MPa (see Holyoke and Kronenberg, 2010). More detailed description of data evaluation and application of the necessary corrections is available in Pec (2014). A correction for stress in salt assemblies, reported by Holyoke and Kronenberg (2010), was not applied because it would produce zero stresses for low σ_1 values in strain rate stepping experiments.

Both as-is and H_2O-added samples have been subjected to two types of axial shortening experiments: 1) constant strain rate and 2) strain rate stepping. Specific conditions for each experiment are listed in **Table 1.** The constant strain rate experiments, carried out at 900 °C, 1 GPa and 10^{-6} s^{-1}, include six higher strain experiments reaching ~30% strain and two lower strain experiments deformed to ~5% strain. The strain rate stepping experiments, performed at 900 °C with strain rate steps of 10^{-5}, 10^{-6} and 10^{-7} s^{-1} and reaching various strains, included six experiments at 1 GPa and two at 1.5 GPa confining pressure. In addition, one as-is sample was only hydrostatically treated (hot-pressed), retaining at 900 °C and 1 GPa for 14 hours, and then quenched.

2.3. Microstructure and texture analysis

Thin sections from deformed samples were analyzed at the Institute of Petrology and Structural Geology, Charles University in Prague, and the Department of Geosciences, University of Tromsø, by means of 1) light microscopy in cross-polarized light, 2) cathodoluminescence (CL) imaging, 3) electron microprobe (EMPA) and element mapping, and 4) electron backscatter diffraction (EBSD) analysis.

Thermionic cathodoluminescence and element maps were acquired using the FEG EPMA JEOL JXA-8530F, equipped with integrated cathodoluminescence spectrometry system xCLent IV, with an accelerating voltage of 15 kV, probe current of 40 - 50 nA and a step size between 0.3 – 1.5 μm. Although for the measurements with step size ≤ 0.5 μm the interaction volume for CL emission is larger than the step size, the acquired maps have significantly better resolution and allow us to observe more details. The reason for that may be in the larger part of the CL signal being emitted from the core region of the interaction volume, while only a smaller part of the signal comes from the rim region (where the density of the penetrated electrons is much lower and the electrons have lost significant part of their energy).

EPMA was also used for backscatter electron (BSE) imaging. EBSD data were acquired using the scanning electron microscope Tescan Vega equipped with NordLys Nano detector (Oxford Instruments), in point-beam mode at 20 kV and 7 nA, and a step size between 0.1 – 1 μm. The EBSD data were collected using the AZtec software (Oxford Instruments) and processed with Matlab toolboxes MTEX 4.5.1. (Hielscher and Schaeben, 2008) and polyLX (Lexa, 2003). Digitized thin section maps of recrystallized domains were constructed using the QGIS open source software.

The grains were reconstructed from EBSD maps by the grain segmentation method of Bachmann et al. (2011). Dauphine twinning and/or pseudo-symmetric boundaries (60° rotation around (0001)) were avoided by changing the trigonal symmetry -3m (321 group) of the EBSD dataset to the hexagonal symmetry (622 group). Grains/subgrains were separated by a boundary in the EBSD maps using a threshold of 3 neighboring pixels with misorientation <2°. We use three types of boundaries in the following text: (1) high angle grain boundaries (HAGB) defined by misorientation angle >10°, (2) low angle subgrain boundaries (LASB) defined by misorientations between 2° and 10°, and (3) low angle inner boundaries (LAIB) defined by misorientation >2°. The difference between the low angle boundaries (2) and (3) is that the subgrain boundaries form closed polygons (subgrains), while the inner boundaries do not. Although the segmentation method allows inner boundaries with misorientation angles >10°, such high misorientations are extremely rare in our samples and therefore the inner boundaries are considered low angle boundaries. Crystallographic orientations of individual grains in EBSD maps are colored using the inverse pole figure color look-up table based on the 622 symmetry. After the segmentation process, the original crystallographic symmetry (-3m) of reconstructed grains and associated EBSD data are used in order to perform the Schmid factor and misorientation analyses (*R. Killian pers. com.*).

The Schmid factor values for dislocation glide were calculated as a product of 1) cosine of the angle between particular glide plane normal and maximum principal stress tensor and 2) cosine of the angle between the glide direction and maximum principal stress tensor (Bouchez and Pecher, 1981; Schmid and Casey,1986; Law et al., 1990) and they consequently range between 0 and 0.5.

The recrystallized grains reconstructed from EBSD maps were used for 2D grain size and shape analyses, carried out using the polyLX (Lexa, 2003) Matlab toolbox. The 2D grain size is given as the diameter of a circle with the area equivalent to a particular grain area. The grains were converted to 3D from the numerical density distribution of the 2D grain size, using the StripStar software (run in Fortran; see details in Heilbronner and Barrett, 2014). The conversion to 3D gives the same results as the Schwartz-Saltykov method (see details in Underwood, 1968; Heilbronner and Bruhn, 1998). The grain shape is described by aspect ratio defined as the momentum-based determination of the longest axis divided by the grain projection in the perpendicular direction.

The preferred orientation and shape analysis of digitized recrystallized domains is manifested by rose diagrams constructed from segmented (same length) boundaries of recrystallized domains (e.g., Lexa, 2003; Heilbronner and Barrett, 2014), solidity of digitized polygons and the shape descriptors deltA and deltP (Heilbronner and Keulen, 2006; Heilbronner and Barrett, 2014). The solidity parameter is defined as the area of a polygon divided by the area of a convex outline (envelope) of a polygon. The deltA displays a ratio between the defect area of a polygon envelope and the area of a polygon, while deltaP is a ratio between the excess length of the polygon perimeter with respect to the outline envelope and the polygon perimeter.

3. Results

3.1. Mechanical behavior of the deformed samples

Mechanical data presented by differential stress vs. strain curves for eight constant strain rate experiments are shown in **Figure 1a**. The curves show similar characteristics for both as-is and H_2O-added experiments, with slightly larger scatter in the loading parts of curves of the H_2O-added samples. The average differential stresses (calculated as the arithmetic mean with one sigma

standard deviation) show slightly higher values for the as-is samples (circles and crosses in **Fig. 1a**). At ~15% strain, where the mechanical behavior is considered closest to steady state flow, the average stresses are 206 ± 21 MPa for as-is and 172 ± 15 MPa for H_2O-added samples. After ~15% strain, the average differential stresses gradually decrease to 185 MPa in the as-is and to 160 MPa in the H_2O-added samples at the final strain (30%). In this strain range, the averaged differential stress of the H_2O-added samples is systematically ~30 MPa lower compared to the as-is samples. Slightly more pronounced softening takes place after ~25% strain in all samples.

Initial strain rate in all eight strain rate stepping experiments was set either to ~10^{-5} s^{-1} or ~10^{-6} s^{-1}. The subsequent slower strain rate step was introduced upon reaching the yield stress and a steady state deformation, based on the stress vs. strain curve (**Fig. 1b**). After a rapid change in stress and its stabilization to a constant value, the slowest strain rate step of ~10^{-7} s^{-1} was initiated. The strain rate changing cycle was repeated at least one more time, but not necessarily in the same order. After

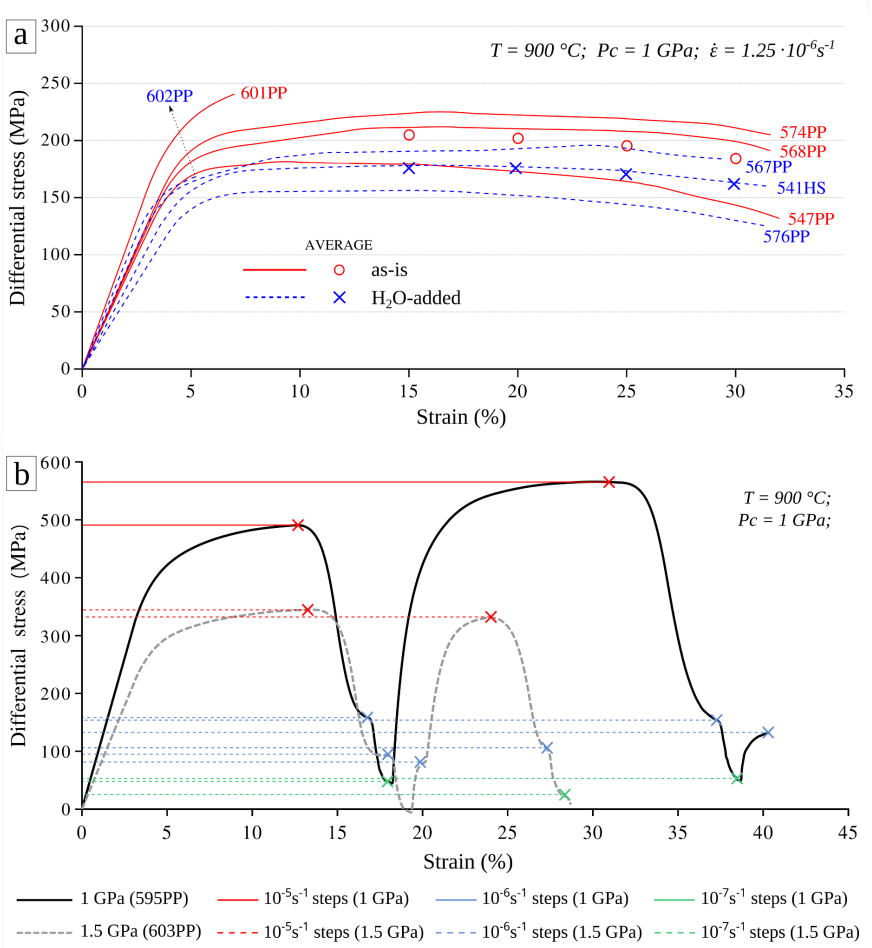

Figure 1. ***a)*** *Stress vs. strain curves for all as-is and H_2O-added constant strain rate experiments. Arithmetic mean of differential stresses is presented by crosses (as-is) and circles (H_2O-added) at 15%, 20%, 25% and 30% strain.* ***b)*** *Example of stress vs. strain curves of two strain rate stepping experiments, carried out at 1 GPa (595PP) and 1.5 GPa (603PP), with strain rates oscillating within predefined steps of $10^{-5}s^{-1}$, $10^{-6}s^{-1}$ and $10^{-7}s^{-1}$. The colored crosses and lines mark values of differential stress used for calculation of stress exponents.*

reaching desired strain (required to achieve a comparable microstructure), the experiments were quenched and depressurized. Flow stress values taken at each step, as presented in **Figure 1b**, were later used for the calculation of stress exponent. The arithmetic mean values of flow stresses at each strain rate step with one sigma standard deviation are presented in **Table 2** for each strain rate stepping experiment. The most significant difference in flow stresses between the as-is and H_2O-added samples at 1 GPa is recorded at the strain rate of 10^{-5} s^{-1} (489 - 548 MPa for as-is and 460 - 505 MPa for H_2O-added (**Table 2**)). The same difference can be seen at the lower stresses of 1.5 GPa experiments (380 MPa for as-is and 337 MPa for H_2O-added). At the strain rate of 10^{-6} s^{-1}, the as-is samples are generally slightly stronger than H_2O-added, while the stresses at 10^{-7} s^{-1} are within the same range. While flow stress of the 1.5 GPa H_2O-added sample at 10^{-7} s^{-1} was only 24 MPa, the stress values of the as-is sample at 10^{-7} s^{-1} steps were not used in our analysis since the flow stress fell below the hit-point (zero stress) value.

Table 1. *Experimental conditions for all experiments. Temperature of 900 °C is constant for all experiments.*

Sample	Experimental setup	H_2O addition (wt %)	Confining pressure (GPa)	Finite strain (%)	Average strain rate (s^{-1})	Deformation time (h)
547PP	Constant strain rate	0	1	32.02	$1.22 \cdot 10^{-6}$	72.8
568PP		0	1	31.6	$1.27 \cdot 10^{-6}$	69.3
574PP		0	1	31.62	$1.24 \cdot 10^{-6}$	70.6
601PP		0	1	7.01	$1.17 \cdot 10^{-6}$	16.6
541HS		0.1	1	31.65	$1.23 \cdot 10^{-6}$	71.3
567PP		0.1	1	29.75	$1.10 \cdot 10^{-6}$	75.9
576PP		0.1	1	31.37	$1.25 \cdot 10^{-6}$	69.7
602PP		0.1	1	5.11	$1.06 \cdot 10^{-6}$	13.5
594PP	Strain rate stepping	0	1	43.67	$9.56 \cdot 10^{-6}$ $1.12 \cdot 10^{-6}$ $1.29 \cdot 10^{-7}$	87.6
595PP		0	1	40.42	$1.26 \cdot 10^{-5}$ $1.34 \cdot 10^{-6}$ $1.35 \cdot 10^{-7}$	55.2
596PP		0	1	30.6	$9.86 \cdot 10^{-6}$ $1.07 \cdot 10^{-6}$ $1.24 \cdot 10^{-7}$	72
581PP		0.1	1	30.58	$1.19 \cdot 10^{-5}$ $1.22 \cdot 10^{-6}$ $1.16 \cdot 10^{-7}$	118.6
582PP		0.1	1	55.77	$9.57 \cdot 10^{-6}$ $1.03 \cdot 10^{-6}$ $1.63 \cdot 10^{-7}$	68.6
584PP		0.1	1	37.64	$1.02 \cdot 10^{-5}$ $1.08 \cdot 10^{-6}$ $1.15 \cdot 10^{-7}$	43.7
603PP		0.1	1.5	28.62	$1.26 \cdot 10^{-5}$ $1.18 \cdot 10^{-6}$ $1.35 \cdot 10^{-7}$	50.1
606PP		0	1.5	26.38	$1.27 \cdot 10^{-5}$ $1.29 \cdot 10^{-6}$	71.1
592PP	Hot-pressing	0	1	-	-	-

Table 2. *Mechanical data from strain rate stepping experiments and stress exponent values calculated separately for each strain rate stepping experiment, including the overall n-values from Fig. 2 and average (arithmetic mean) values with one sigma standard deviation. Flow stress values are presented as mean values with one sigma standard deviation, except for single values. T = 900 °C.*

Sample	594PP	595PP	596PP	581PP	582PP	584PP	606PP	603PP
H_2O addition (wt %)	0	0	0	0.1	0.1	0.1	0	0.1
Pc (GPa)	1	1	1	1	1	1	1.5	1.5
Mean flow stress at $10^{-5}s^{-1}$ (MPa)	548 ± 74	527 ± 53	489 ± 73	501	505	460 ± 14	380 ± 73	337 ± 9
Mean flow stress at $10^{-6}s^{-1}$ (MPa)	193 ± 4	149 ± 12	183 ± 11	181 ± 52	170	157 ± 10	77 ± 41	93 ± 11
Mean flow stress at $10^{-7}s^{-1}$ (MPa)	83 ± 4	50 ± 7	73 ± 19	58	69	65	-	23
n	2.175	1.805	2.021	2.147	2.169	1.988	1.454	1.77
n overall	1.938			2.128			-	
n average	2.003 ± 0.186			2.101 ± 0.098			-	

3.2. Strain rate stepping experiments and determination of stress exponent

Six strain rate stepping experiments performed at 1 GPa and two at 1.5 GPa confining pressure were used to determine the stress exponent. The experiments have shown reproducible results for both as-is and H_2O-added samples, reaching similar flow stresses upon repeated strain rate changing cycles (**Fig. 1b**). The peak differential stresses, used in the calculation, were determined separately for each strain rate step (**Fig. 1b, Table 2)**. The exact strain rate for each step was determined as total strain accumulated during the particular step divided by its duration (a period between σ_1 motor speed changes). The linear regression fit through the experimental data plotted as log $\dot{\varepsilon}$ vs. log σ indicates the $\dot{\varepsilon} \propto \sigma^n$ relationship, allowing the determination of stress exponent (n), with the error of the fit expressed by a coefficient of determination R^2 (**Fig. 2**). The linear regression fit through the three as-is experiments at 1 GPa confining pressure indicates n-values of 1.94 and for the three H_2O-added experiments 2.13. The as-is experiment at 1.5 GPa confining pressure showed a lower n-value (1.45) than the H_2O-added (1.77; **Fig. 2**). The linear regression fit for the as-is 1.5 GPa experiment, however, suffers from fewer data points and relatively large scatter (with R^2 = 0.908), and therefore the n-value of 1.45 is less certain. The n-values were also calculated separately for each experiment and listed in **Table 2**.

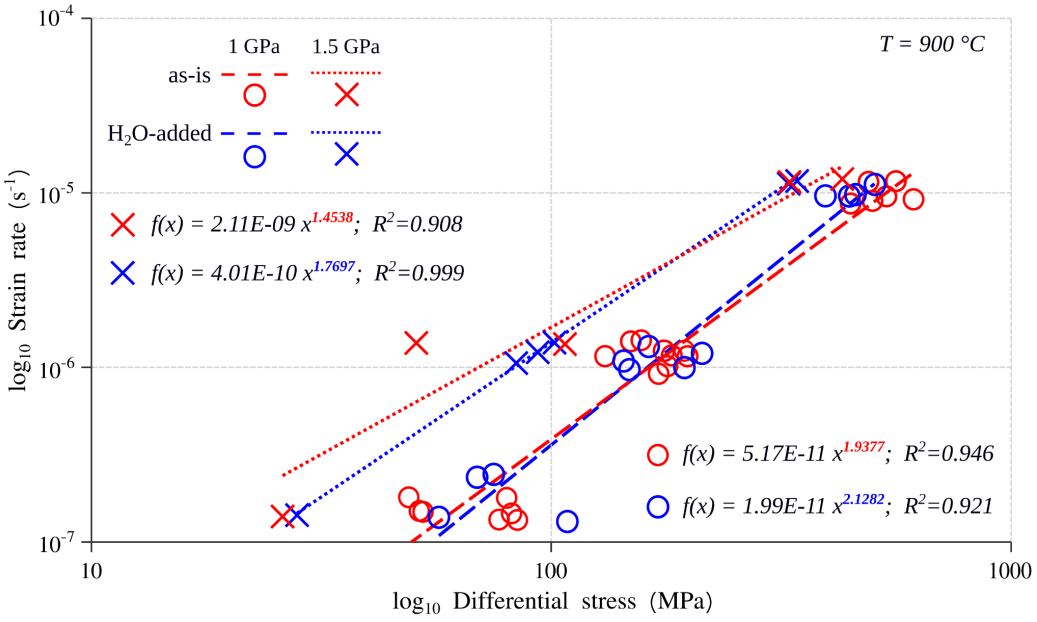

Figure 2. *Log strain rate – log differential stress relationship used to determine stress exponent (n) from the strain rate stepping experiments. Results from as-is experiments are plotted in red color and H_2O-added in blue. Results for 1 GPa experiments are presented by circles and for 1.5 GPa by crosses, with dashed and dotted linear regression fit, respectively. Stress exponent (n) values are highlighted using the same color coding. The error of the linear regression fit is expressed by a coefficient of determination R^2.*

3.3. Microstructure of the starting material

In order to evaluate microstructures developed in our deformed samples, we determined those of the starting material first. The average grain size in the selected Tana quartzite samples is ~200 µm (Negre et al., 2021). The grains are equant, forming a mosaic-like microstructure with no crystal preferred orientation nor shape preferred orientation observed (**Fig. 3a**). Cathodoluminescence (CL) imaging reveals that the individual quartz grains consist of rounded cores (shades of yellow and orange or sometimes cyan-blue luminescence), which are irregularly overgrown by a cement rim (dark brown luminescence, sometimes interspersed with yellow) without change in crystallographic orientation between the cores and rims (cf. **Fig. 3a-b**). The CL colors are explained in more detail in **Appendix 3** in terms of wavelengths and intensities of emitted luminescence. The cores correspond to original sand grains while cement represents the infill of pore space, which is in line with the sedimentary origin of the studied quartzite (Johnson et al., 1978). The original sand grains are dominantly single crystals with sporadic occurrence of polycrystalline aggregates.

The Al and K element maps obtained by EMPA show pronounced concentration maxima surrounding the original sand grains (**Fig. 3c-d**). **Figure 3e-h** demonstrates spatial overlap of Al and K concentration maxima with layers and clusters of accessory mineral phases, identified by EMPA as muscovite and illite. These phases represent the largest portion of impurities, occurring commonly at the interface between the sand grains and cement, and less often along the grain boundaries. The impurity regions usually appear as mixtures of the two phases, in the form of ultra-small needle- or sheet- like particles, preventing the exact determination of their chemical composition (**Fig. 3h**). Rarely, biotite and K-feldspar inclusions up to several µm in size occur within the quartz grains. Clusters rich in Fe-oxides were also found in the impurity regions, as well

as tiny inclusions of zircon, apatite, xenotime, monazite, goyazite and rutile. The Na, Fe and sometimes Ca element maps show the same distribution as Al and K, but with less prominent relative concentration differences. For this reason, the Al and K EMPA maps were chosen to trace the distribution of the impurity phases throughout the studied samples.

It should be noted that the distribution of Al and K concentration maxima in the EMPA element maps (**Fig. 3c-d**) is spatially exaggerated due to the large step size and sensitivity of the method. Therefore, these element maps do not display real proportions of the impurity phases but rather demonstrate their spatial arrangement. The more realistic spatial extent and position of the impurity regions is provided by the high resolution Al map of a much smaller area (**Fig. 3g**; cf. with corresponding marked rectangle region in the low resolution EMPA map in **Fig. 3c**). Together with the optical, CL, and BSE images (**Fig. 3e-h**), it demonstrates that layers of impurity phases are typically less than 1 μm thick, with sporadic thicker clusters of up to 30 μm in size. Based on the high resolution BSE, CL and EMPA maps, the volumetric proportion of the impurity phases in the starting material is estimated to be < 1%. Besides its concentration peaks, slightly elevated Al concentrations are systematically observed in the cement regions (white arrows in **Fig. 3c**). Here, the Al enrichment is likely related to the cementation/diagenesis processes occurring either via precipitation of tiny particles of Al-bearing phases from a fluid, or via Al-Si substitution in the newly grown cement. Presence of sparse Fe-rich clusters in the impurity regions may indicate that a relatively small proportion of total OH^- in the studied samples could be released due to $FeOH_x$ disintegration. However, the optical observation of the samples indicates a low content of Fe-bearing mineral phases.

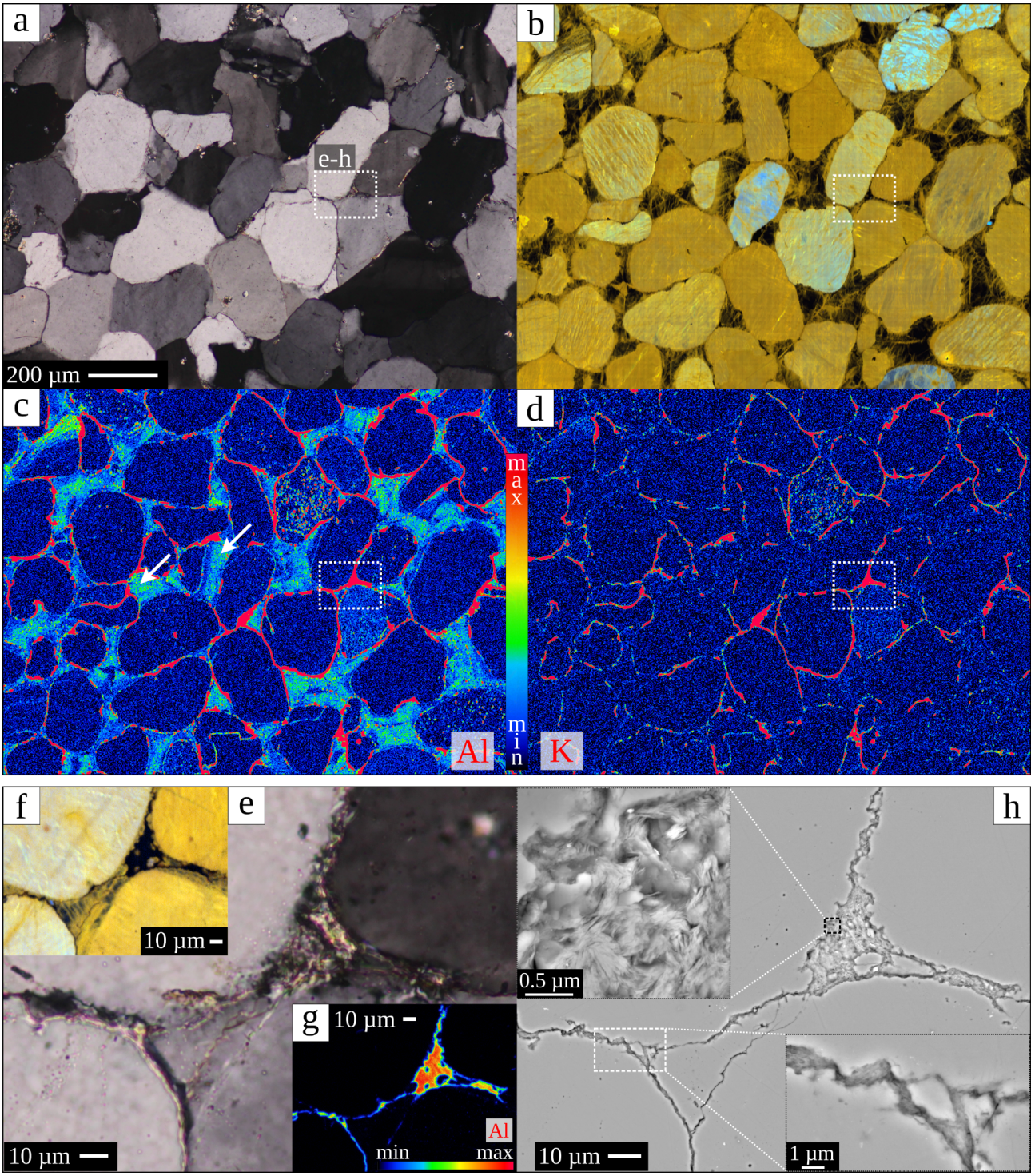

Figure 3. ***a-d)*** *Representative mosaic-like microstructure of the starting material;* ***e-h)*** *higher resolution images focusing on the mica-impurity region in the cement, marked by white dotted rectangle in (a-d). White arrows in (c) point to the elevated Al concentrations in the cement regions with respect to the original grains. (a), (e): cross-polarized light images; (b), (f): CL images; (c), (g): microprobe (EMPA) element maps of Al; (d): EMPA element map of K; (h): BSE image. Scale for images (a-d) is presented in image (a). CL images distinguish sand grains (light yellow, light blue) and cement (dark brown). Concentration scale in EMPA element maps is relative.*

3.4. Microstructures of deformed samples

3.4.1. Low strain samples

Samples 601PP (as-is), deformed to 7%, and 602PP (H_2O-added), to 5% strain (**Fig. 1a**), have provided valuable insight into the initial stages of deformation. The as-is sample shows local cracking and onset of recrystallization mainly in triple and quadruple junctions of quartz grains, occurring mostly at the grain boundaries (marked rectangles in **Fig. 4**). Compared to the starting material, the original quartz grains exhibit a weak sweeping undulatory extinction and their boundaries become slightly irregular and occasionally lobate (cf. **Figs. 3a** and **4a**). These deformation features are accompanied by a prominent change in luminescence to blue color observed mainly in narrow zones along the grain boundaries and in cracked regions (**Fig. 4b**). The blue CL color that appears in the deformed samples shows a dominant emission band at 450 nm wavelength which is in clear contrast to the dominance of 650 nm wavelength band in the original sand grains and cement (**App. 3**).

Despite the fact that the H_2O-added sample was subjected to slightly lower strain than the as-is sample, it exhibits significantly better-developed deformation features (cf. **Figs. 4a** and **5a**). Compared to the as-is sample, the original grains in the H_2O-added sample exhibit a higher degree of undulatory extinction, which often occurs in patchy patterns. Many irregular boundaries, revealing lobate embayments, show prominent blue luminescence (light blue arrows in **Fig. 5a-b**) that document the mobility of grain boundaries. The best examples of such embayments can be observed along boundaries that are approximately parallel to the σ_1 principal stress. Local cracking is often difficult to recognize in cross polarized light (white arrows in **Fig. 5a)**, because many cracks are healed after the experiment. The healed cracks are marked by the blue luminescence, revealing cracks that cut across both cement and original sand grains (highlighted strip and white arrows in **Fig. 5c**). Most of these longitudinal cracks are (sub)parallel to the σ_1 principal stress, suggesting tensile mode I crack opening. They locally coincide with crack networks, where aggregates of smaller new individual grains can be observed (red arrows in **Fig. 5a** and **c-d**). It is important to emphasize that there are no signs of such extensive cracking during increase in P-T-conditions (pumping-up stage of experiment), as documented by the lack of such microstructures in the hot-pressed as-is sample 592PP, shown in **Appendix 4**. In this isostatically pressurized and heated sample, appearance of the blue luminescence is not observed, neither in original sand grains nor the cement.

The onset of recrystallization is significantly more pronounced in the H_2O-added low strain sample than in the as-is one. Networks of the healed cracks in the H_2O-added sample typically show small misorientations marked with low angle (<10°) boundaries, separating misoriented domains in the original quartz grains (see highlighted crack zone and white arrows in **Fig. 5d**). Moreover, regions of higher crack density show fragmentation of the original grains resulting in development of smaller, fragment grains characterized by both low angle and high angle (>10°) misorientations (red arrows in **Fig. 5d**). An example of recrystallization and reconstitution of material by cracking, where the newly formed fragments are separated by blue-luminescent rims is shown in **Figure 6**. These fragments preserve original brown cement-related luminescence in their cores (orange arrows in **Fig. 6a**) and are commonly associated with channels and pockets, which are filled by non-diffracting material that shows no luminescence (yellow arrows in **Fig. 6**). A reddish luminescence that sometimes appears in these channels and pockets corresponds to epoxy infill.

Spatial coincidence of higher crack density regions with appearance of small independent grains indicates a role of cracks in the recrystallization of low strain samples.

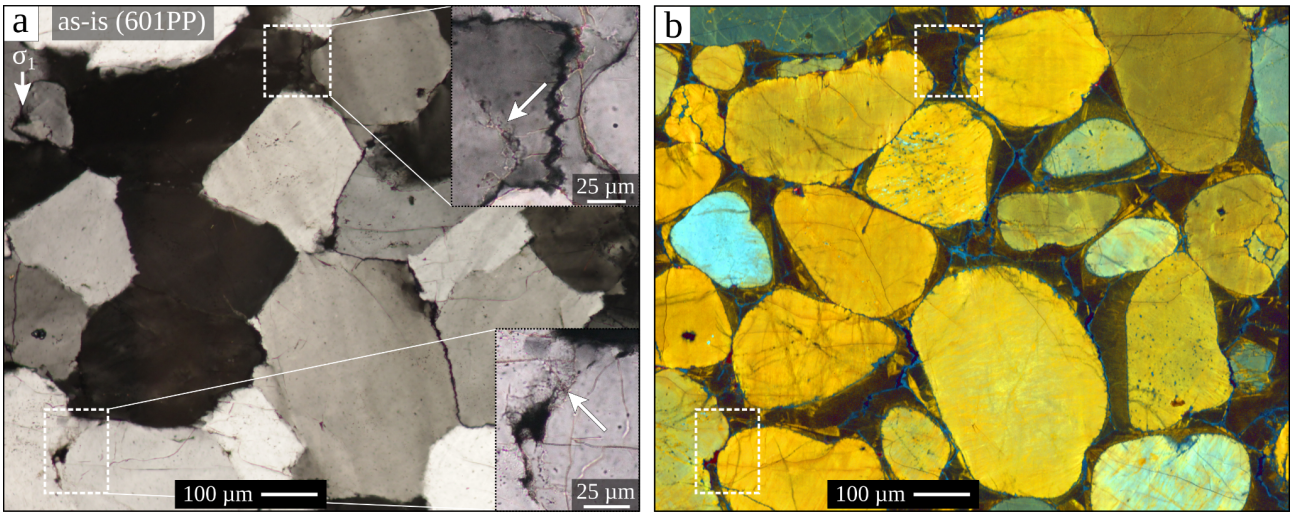

Figure 4. *Microstructure of the low strain (7%) as-is sample 601PP shown in:* ***a)*** *cross-polarized light and* ***b)*** *CL image. White dashed rectangles highlight locally cracked regions and associated onset of recrystallization. White arrows in insets point to small networks of cracks. The CL image shows original sand grains in yellow or light blue, cement in dark brown, deformation zones of reconstituted/recrystallized material in blue.*

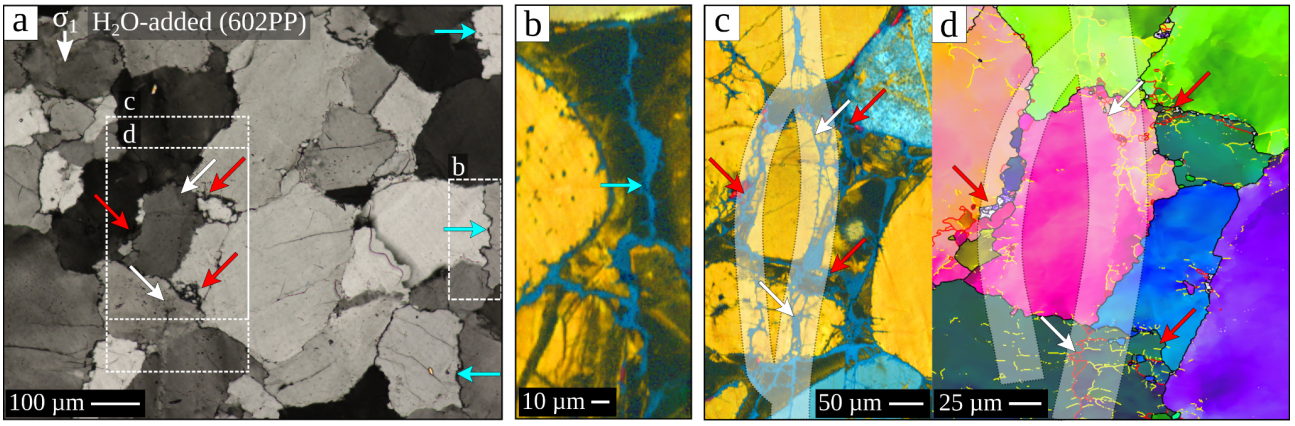

Figure 5. ***a)*** *Microstructure of the low strain (5%) H_2O-added sample 602PP in cross-polarized light. The white dashed rectangles mark locations of images in (b-d).* ***b)*** *CL image zooming the lobate embayments along the original grain boundaries (cyan arrows);* ***c-d)*** *CL image (c) and EBSD map (d) focusing on longitudinal through-going crack parallel with maximum principal stress σ_1 (highlighted) and associated smaller cracked domains with onset of recrystallization (red arrows) and healed cracks (white arrows). The EBSD map shows individual grains with their crystallographic orientation colored by the inverse pole figure scheme in Fig. 8c; boundaries are marked by black lines for HAGBs, red lines for LASBs and yellow lines for LAIBs.*

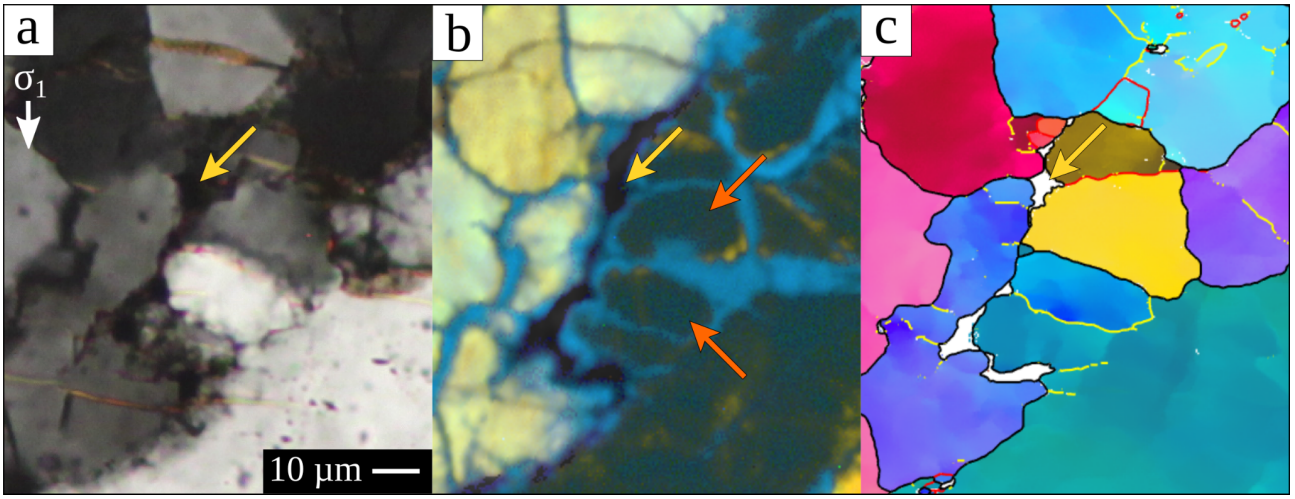

Figure 6. *Example of a domain of cracked fragment grains in the low strain (5%) H_2O-added sample 602PP, in* ***(a)*** *cross-polarized light,* ***(b)*** *CL image and* ***(c)*** *EBSD map. Yellow arrows point to an amorphous pocket that shows no luminescence (black) nor diffraction; orange arrows show cracked fragment grains with original cement-related luminescence and blue-luminescent rim. Details for the EBSD map in (c) are explained in the caption to Fig. 5, and the coloring scheme provided in Fig. 8c. Scale for all images is presented in (a).*

3.4.2. Higher strain samples

All as-is and H_2O-added samples shortened by ~30% show barrel-like shapes (**Fig. 7a**). The most deformed parts of the samples correspond to the position of the thermocouple, where the temperature is expected to be the highest. The uppermost parts are the least deformed, with only minor signs of deformation. In 3D, the least deformed parts have conical shapes with the U-shape 2D crosscut (yellow dotted line in **Fig. 7a**). This distinction is in a good agreement with the contrasting microstructures observed in the middle-lower and upper parts of the samples (cf. images (1-2) in **Fig. 7b** and **c**). The microstructure in the least deformed upper parts is very similar to the microstructure of the starting material, including grain sizes and shapes, luminescence and position of concentration maxima in Al and K EMPA element maps (cf. **Figs. 3a-d** and **7b**). The intensity of deformation gradually increases towards the most deformed middle to lower parts of the samples as documented by (1) increasing amount of flattening and associated undulatory extinction of the original grains, (2) higher degree of recrystallization, (3) more abundant cracks or regions with high crack density, and (4) associated redistribution of Al and K rich accessory phases (cf. **Fig. 7b** and **c**). The higher strain samples also show more unloading cracks (visible in **Fig. 8a** and **e**), which are open, straight and perpendicular to the σ_1 principal stress direction, and often crosscut several neighboring grains. These cracks are excluded from further description.

In addition to intense sweeping and patchy undulatory extinction, the most deformed parts show strong shape preferred orientation of the original grains demonstrated by CL imaging in **Figure 7c**. The long dimensions of deformed grains are perpendicular to the maximum stress σ_1 direction. A relatively large portion of cement shows zones of prominent blue luminescence, which occasionally also crosscut the original sand grains (image (2) in **Fig. 7c**). The blue luminescence spatially coincides with deformation zones occupied by small grains with a size up to 15 µm, as well as with intensely cracked regions or individual cracks (blue, red and white ellipses, respectively, in **Fig. 7c)**.

Compared to the low strain H_2O-added sample, where cracks are largely healed, the higher strain samples more frequently show cracks which are only partly healed (cf. white arrows in **Fig. 5a,c** and images (1-2) in **7c**). The Al and K concentration maxima in the most deformed parts occur in smaller or larger clusters in the cement regions and locally also within the original sand grains (cf. images (3-4) in **Fig. 7b** and **c**).

The clusters of Al and K concentration maxima spatially overlap with high crack density regions (red ellipses in **Fig. 7c**) where channels and pockets filled by amorphous material usually occur (e.g., in **Fig. 8**). These amorphous channels and pockets correspond to narrow channels and wider gaps of up to 30 μm in size, which show no luminescence, no diffraction, maxima in concentration of Al and K (Fig. **8a-d**), and small circular bubbles inside the amorphous material (brown arrows in **Fig. 8e**). The amorphous channels and pockets are closely associated with cracks that cross-cut both cement and original sand grains (white arrows in **Fig. 8a-d**). Healed or partly healed trans-granular cracks that often separate cement from the original sand grains are usually marked by low to high angle boundaries and are often associated with few smaller grains visible in the EBSD map (see the white arrow to the left in **Fig. 8a-c**).

In the high crack density regions, typically associated with amorphous channels and pockets, most of the recrystallized grains correspond to crack-related fragments (red circles in **Figs. 8a-c** and **9**). These fragment grains often show angular shapes, with blue luminescent faceted overgrowth rims and locally preserved original brown luminescence in their cores (green arrows in **Fig. 8e-f**; orange arrows in **Figs. 8b** and **9**). Although most of the fragment grains are separated by high angle boundaries, some of these grains only show low angle (<10°) misorientations to the original grains (white arrows in **Fig. 8e-f**). In the crack-related recrystallized domains associated only with minor amorphous channels (red circle and yellow arrows in **Fig. 9b**), cracked fragments of cement are often overgrown by new material, where the individual fragments meet, exposing bright boundaries in monochromatic CL images (gray arrows in **Fig. 9b**).

Aside from fragmentation in the high crack density regions, recrystallization also occurs in domains with extremely low crack density (blue ellipses in **Figs. 7c, 8a-c and 9**). These domains are not associated with amorphous channels or pockets; hence they are recognized by low concentrations of Al and K (images (3-4) in **Fig. 7c**) and are described in detail in the following sections.

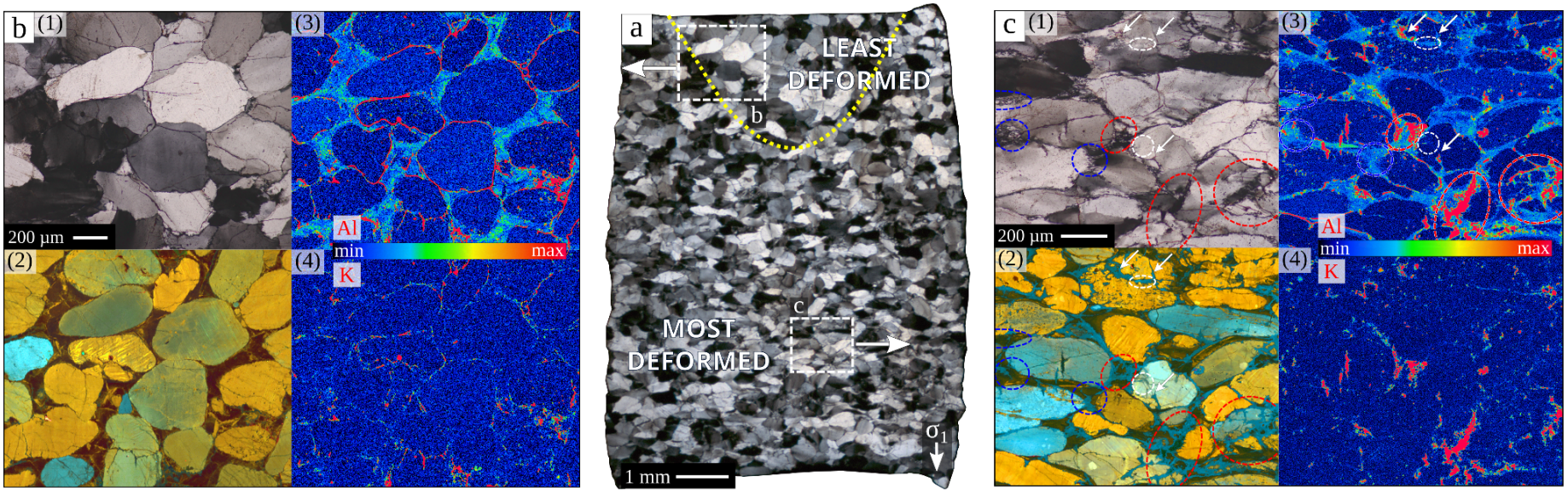

Figure 7. *Comparison of microstructures in the least and the most deformed parts of the higher stra. on the example of as-is sample 568PP.* ***a)*** *Cross-polarized scan of the entire sample thin sectio locations (white dashed rectangles) of microstructures from* ***(b)*** *the least and* ***(c)*** *the most deformed yellow dotted line approximately delimits the least deformed portion of the sample. Images microstructures in cross-polarized light, images (2) in CL, images (3) in Al element maps and imag element maps. Red and blue ellipses in (c) mark recrystallized domains characterized by higher crack densities, respectively. White ellipses and arrows mark domains of healed crack networks healed cracks, respectively. Scales for images in (b) and (c) are provided in the images (1).*

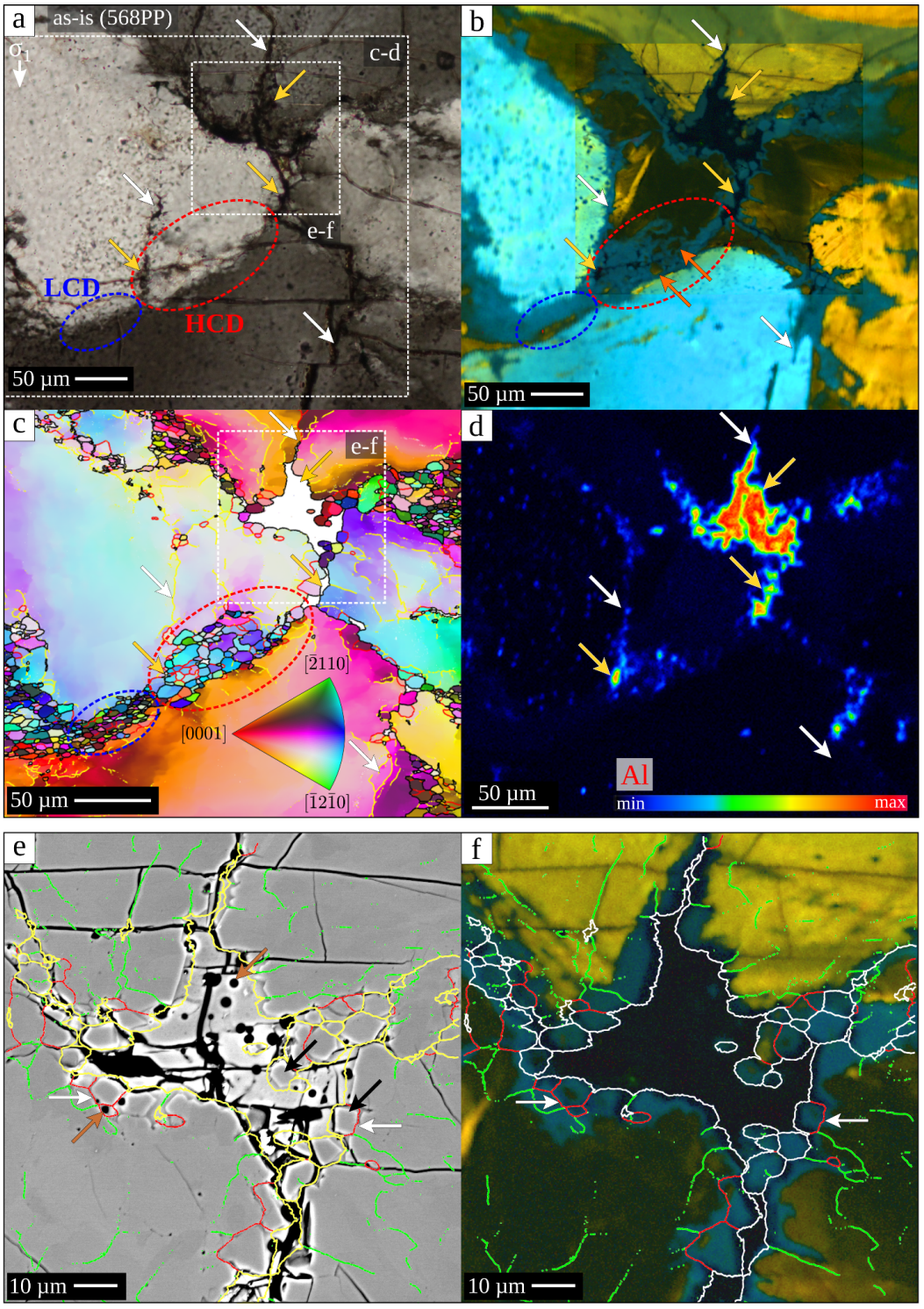

Figure 8. *Microstructural features in the most deformed part of the higher strain as-is sample 568PP shown in* ***(a)*** *cross-polarized light,* ***(b)*** *and* ***(f)*** *CL image,* ***(c)*** *EBSD map,* ***(d)*** *Al element map and* ***(e)*** *BSE image. White dotted rectangles in (a) and (c) mark location of images (c-f). White and yellow arrows in (a-d) point to cracks and amorphous pockets and channels, respectively. Orange arrows in (b) point to recrystallized grains that preserve the original cement-related luminescence. Blue and red ellipses in (a-c) highlight recrystallization in low (LCD) and high (HCD) crack density regions. (e-f) Focus on the amorphous pocket and its surrounding, with superposed low and high angle boundaries (LASB in red, LAIB in green, HAGB in yellow and white). (e) Shows light gray amorphous infill of the pocket, with bubbles (brown arrows) and idiomorphic recrystallized grains and subgrains (black arrows) characterized by blue luminescence in (f). White arrows in (e-f) point to subgrain boundaries filled with amorphous material, separating cracked fragment grains from the original grains.*

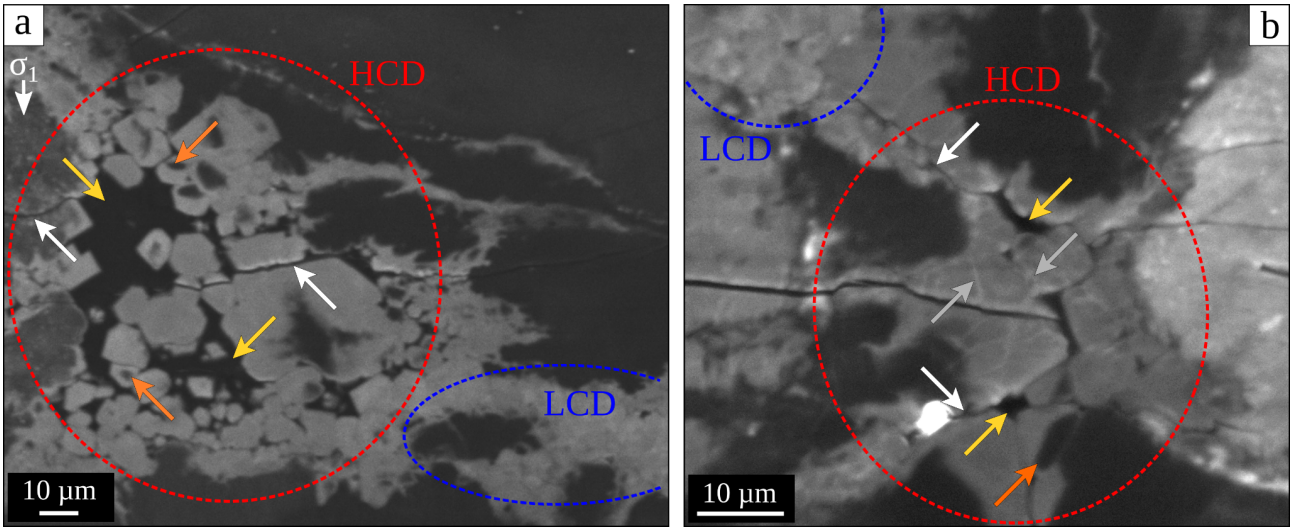

Figure 9. *High resolution monochromatic CL images of HCD and LCD recrystallized regions. HCD regions show examples of* ***(a)*** *larger amorphous pockets and* ***(b)*** *smaller channels. The recrystallized grains in the vicinity of amorphous pockets and channels show idiomorphic shapes. The brighter gray shades in recrystallized domains correspond to the blue luminescence in the RGB CL images, while darker shades correspond to the dark brown. Amorphous material is non-luminescent (black). Orange arrows point to original cement-related luminescence preserved in the cores of some grains, yellow arrows to amorphous pocket/channels, white arrows to open cracks and light gray arrows to straight boundaries of recrystallized grains in a highly cracked domain in (b).*

3.5. Intracrystalline deformation of the original grains

Original quartz grains in the most deformed parts show a high degree of undulatory extinction (image (1) in **Fig. 7c**) caused by distortion of the crystal structure and development of low angle boundaries (LAIBs and LASBs; **Fig. 8c**). The suspected intracrystalline plasticity (dislocation glide) was tested in the lower crack density regions of original grains, by evaluating their geometric potential to activate specific slip systems (Schmid factor analysis), together with distribution of correlated misorientation axes across the LAIBs and LASBs. An example of such comparison based on the EBSD data from the map in **Figure 8a** is shown in **Figure 10**.

The observed distribution of misorientation axes for both LASBs and LAIBs (**Fig. 10c**) showed the dominance of {m}<a> slip, less frequent {r}<a>, {z}<a>, and the least frequent {c}<a> (**Fig. 10a** and **c**). The dominance of {m}<a> slip is well demonstrated in grain 3, despite its lower Schmid factor 0.3 compared to ~0.45 for {c}<a> and {z}<a>, and in grain 4 (comparable activity of {m}<a>, {z}<a> and {c}<a>), despite its considerably lower Schmid factor 0.19 compared to 0.35 for {z}<a> and 0.47 for {c}<a>. The only example of near absent apparent activity of {m}<a> is shown in grain 2 where its Schmid factor approaches zero. The grain 2 thus shows dominant apparent activity of {c}<a> and rhomb<a> slip systems.

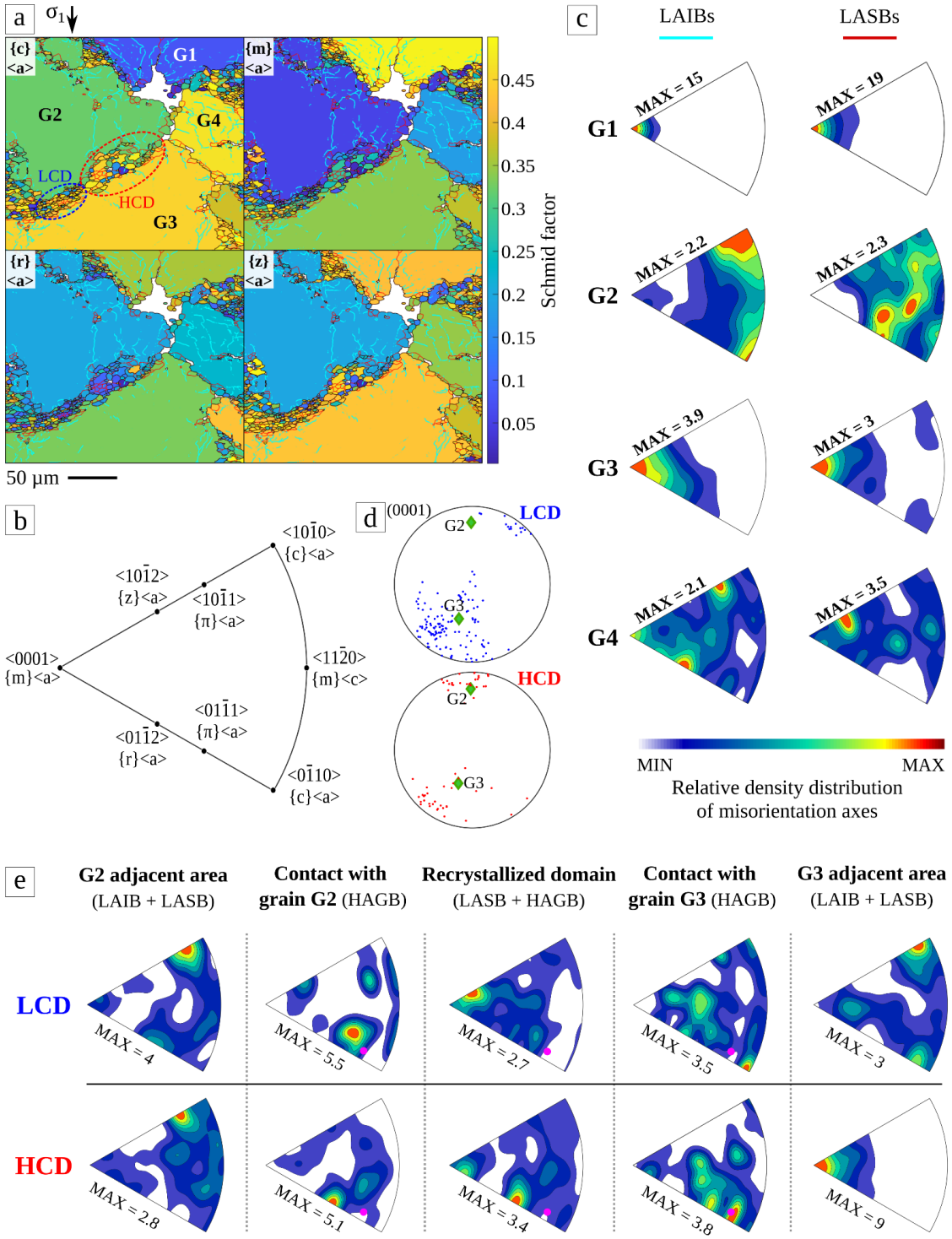

Figure 10. *Schmid factor and misorientation analysis of the original and recrystallized grains from the region shown in Fig. 8a-d.* ***a)*** *EBSD grain maps colored by Schmid factor values for {c}<a>, {m}<a>, {r}<a> and {z}<a> slip systems. LAIBs are shown in blue and LASBs in red. Recrystallized LCD and HCD domains are marked by blue and red ellipses, respectively.* ***b)*** *Inverse pole figure (IPF) for -3m symmetry shows expected positions of boundary misorientation axes related to a specific slip system and assuming tilt boundaries only;* ***c)*** *quartz IPFs show distribution of misorientation axes determined from correlated misorientation across LAIBs and LASBs within the original grains G1-G4 in (a);* ***d)*** *pole figures with orientation of poles to (0001) planes of grains G2 and G3 (green diamonds), and of associated recrystallized grains from LCD (blue dots) and HCD (red dots) domains;* ***e)*** *IPFs for -3m symmetry showing distribution of misorientation axes from correlated boundary across LAIB, LASB, and HAGB boundaries in the LCD and HCD recrystallized domains, in adjacent portions of the original grains G2 and G3, and across the contact between recrystallized and original grains; pink dots mark misorientation axis between G2 and G3. Contours in the IPFs correspond to density distribution of misorientation axes with their maximum determined for each inverse pole figure.*

3.6. Recrystallized domains and recrystallization mechanisms

The microstructure of the most deformed parts in all as-is and H_2O-added samples reveals that recrystallization takes place mainly in the cement regions, between the plastically deformed and locally cracked original sand grains. The recrystallized domains generally consist of (1) small newly formed grains, (2) non-recrystallized relics of cement or original sand grains, and (3) amorphous channels and pockets (**Figs. 8** and **9)**. Since the previous sections documented both widespread cracking and grain fragmentation, and the crystal plastic deformation of the original quartz grains associated with subgrain rotation, the question arises which of the two processes is more responsible for the observed recrystallization.

Two distinct types of recrystallized domains have been identified in the higher strain samples. They differ by the abundance or lack of cracks, position and geometry with respect to original grains, relation to amorphous channels and pockets, as well as luminescence and crystallographic orientation relations of recrystallized grains. As the occurrence of cracks is the most distinguishing feature, mostly visible in BSE observation, two different domains of recrystallization are referred to as low crack density (LCD) and high crack density (HCD) recrystallized domains (**Fig. 11d-f**). The LCD domains (blue ellipses in **Figs. 7c**, **8a-c**, **9** and **11a-f**) usually occur along original grain boundaries that are inclined with respect to the σ_1 principal stress direction. Sometimes they also occur at corners of original grains (e.g., LCD-3 in **Fig. 11c**). The HCD domains (red ellipses in **Figs. 7c**, **8a-c**, **9** and **11a-f**) are typically associated with triple and quadruple junctions of the original grains. The HCD domains always occur in association with amorphous channels and pockets or smaller voids sometimes filled with epoxy (appears red in the CL), while LCD domains usually lack these features (cf. red and blue ellipses in **Fig. 11d-f**).

The differences in recrystallized grain size and shape in LCD and HCD domains are presented on the example of the EBSD results shown in **Figure 11c**, using (1) 2D diameters of cross-sectional areas of the grains, shown as the number-weighted distribution $h(d)$ (**Fig. 12a**), (2) 3D diameters of the spheres calculated from the 2D data, shown as the volume-weighted distribution $v(D)$ (**Fig. 12b**; e.g., Heilbronner and Bruhn, 1998; Heilbronner and Kilian, 2017) and (3) aspect ratio determination by the longest axis divided by the grain projection in the perpendicular direction (**Fig. 12c**).

Recrystallized grains in LCD domains tend to have a smaller and more uniform size. They are typically more rounded in shape and have higher aspect ratios compared to those of HCD recrystallized grains. The HCD recrystallized grains are more irregular, with both rounded and angular shapes and more heterogeneous in size (cf. blue and red regions in **Figs. 8c, 11c** and **12a-c**). The 2D grain size in the analyzed LCD domains rarely exceeds 7 μm, showing a standard log-normal distribution with a mean value of 3.08 μm. The grain size distribution in the HCD domains shows lower kurtosis with larger grain sizes of >11 μm. However, the mean value of 4.14 μm in HCD domains is only slightly bigger than in LCD (**Fig. 12a**). More prominent differences are apparent in the 3D grain size distributions where LCD grains follow a log-normal distribution with mode value of 4.2 μm, where HCD grains show an irregular (scattered) distribution with mode value of 6.7 μm (**Fig. 12b**). The aspect ratio of recrystallized grains in all LCD and HCD domains was used to describe the grain shape differences in the two domains (**Fig. 12c**). Recrystallized grains in the LCD domains show more elliptical shapes with an average aspect ratio of 2.2 while in the HCD domains the grains are more equiaxial with average aspect ratio of 1.5.

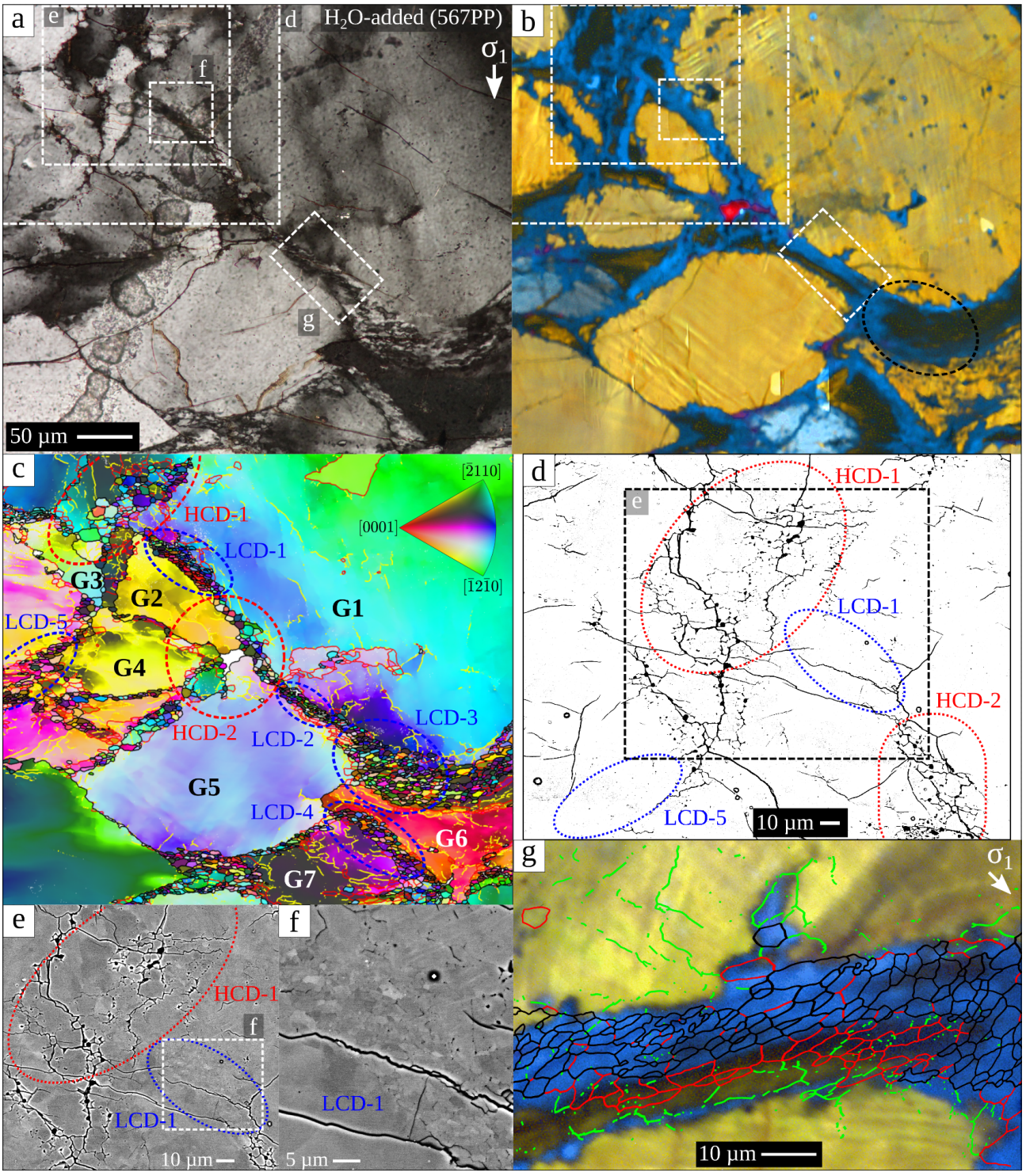

Figure 11. ***a-c)*** *Recrystallization domains in the higher strain (30%) H_2O-added sample 567PP shown in (a) cross-polarized light, (b) CL image and (c) EBSD map. Recrystallization related to LCD and HCD domains is marked by blue and red ellipses, respectively. Black ellipse in (b) highlights the position of domain LCD-3, specific by preserved original brown luminescence in LCD-recrystallized grains. The white dotted rectangles in (a-b) mark the location of images in (d-g). Step size used for acquiring EBSD map in (c) is 0.4 µm. Scale for images (a-c) is presented in (a).* ***d-f)*** *BSE images demonstrate the difference in void and crack density in LCD (blue ellipses) and HCD (red ellipses) domains. Image in (d) is modified for brightness and contrast in order to emphasize visibility of the cracks. Horizontal and semi-horizontal straight cracks result from unloading.* ***g)*** *Magnified CL image showing domain LCD-2 from (a-c), with superposed HAGBs (black), LASBs (red) and LAIBs (green).*

Similar crystallographic orientation relationships are observed for original grains and neighboring recrystallized grains in LCD and HCD domains (**Fig. 10d**). However, the LCD domains show a more systematic orientation relationship between recrystallized and original grains (**Figs. 10d** and **12d**). HCD domains generally show higher scatter in orientation of recrystallized grains and lower correlation to the original grain orientation (**Fig. 12d**).

Analysis of crystallographic misorientation in LCD and HCD recrystallized domains was performed in both as-is and H_2O-added samples to identify the possible operation of dislocation creep. The systematic analysis of correlated misorientation across the different types of boundaries has been carried out along a profile from one original grain to the other, across the recrystallized domain. The misorientation axes in the inverse pole figures were plotted separately for (1) low angle boundaries (LAIBs and LASBs) from the smaller portions of original grains adjacent to the recrystallized domains, (2) high angle grain boundaries (HAGB) across the contact between original and recrystallized grains, and (3) low and high angle boundaries (LASB and HAGB) between grains and subgrains in the recrystallized domains (**Figs. 10e** and **12e**). For this analysis, one LCD and one HCD domain from the as-is sample 568PP (**Figs. 8c** and **10a**) and two LCD(-2 and -4) and one HCD(-1) domains from the H_2O-added sample 567PP (**Fig. 11c**) were selected as examples.

The LCD domains generally show a good match in misorientation axes determined for the original and recrystallized grains, as well as for the contact HAGBs, while the HCD regions lack this match (**Figs. 10e** and **12e**). For example, the HAGB contact of the LCD recrystallized domain with G3 shows misorientation axes in similar positions as for the LAIBs and LASBs in G3, while the contact with G2 shows position of misorientation axes close to the location of the misorientation axis between G2 and G3 near the z-rhomb axis (pink dots in inverse pole figures in **Fig. 10e**). This observation suggests that these LCD-recrystallized grains are formed by SGR, originating from G3 and not to G2 (**Fig. 10d**). Even though the HCD-recrystallized grains from the same map (**Fig. 10a**) originate mostly from the grain G2 (**Fig. 10d**; overlap of misorientation axis maxima at G3-HCD contact and the location of the misorientation axis between G2 and G3 in **Fig. 10e**), the correlation of the misorientation maxima between G2 and the recrystallized domain is less-defined, which suggests a reduced contribution of SGR. LCD regions presented in **Figure 11c** show similar correlation in distributions of misorientation maxima across the contacts with the original grains, while lack of clear misorientation relations at the HCD domain again suggests their origin from cracking and local fragmentation (cf. LCD and HCD regions in **Fig. 11d-f**). This situation is compatible with less-defined orientation relationships between original and HCD-recrystallized grains (**Fig. 12d**). More detailed description of observed misorientation relationship is provided in **Appendix 5**.

The change to blue luminescence systematically differs for the LCD and HCD recrystallized domains. The HCD domains frequently show individual small recrystallized grains and subgrains with blue luminescence (**Fig. 8b,f**) in which sometimes the original, mostly cement-related brown luminescence can be preserved in the cores of larger recrystallized grains (orange arrows in Figs. **8b** and **9a**). Smaller recrystallized grains and subgrains in HCD domains typically show blue luminescence (**Fig. 8b,f**). In contrast, recrystallized grains in the LCD domains in some cases exhibit the original luminescence (e.g., lower part of LCD domain in **Fig. 8b** and LCD-3 (black ellipse) in **Fig. 11b**), but in most cases, the LCD grains show blue luminescence (e.g., LCD-1,

LCD-2 and LCD-4 in **Fig. 11b**). Detailed luminescence image of LCD-2 overlain with boundaries in **Figure 11g** shows that most of the recrystallized grains (black outlines) turned blue while subgrains (red outlines) in the lower part of the recrystallized domain did not. The observed differences in luminescence of the LCD and HCD domains, their orientation relationships, and their different shape and size relationships, demonstrate that the recrystallization in the HCD domains is dominantly initiated by cracking and fragmentation, whereas the recrystallization in the LCD domains is initiated by subgrain rotation.

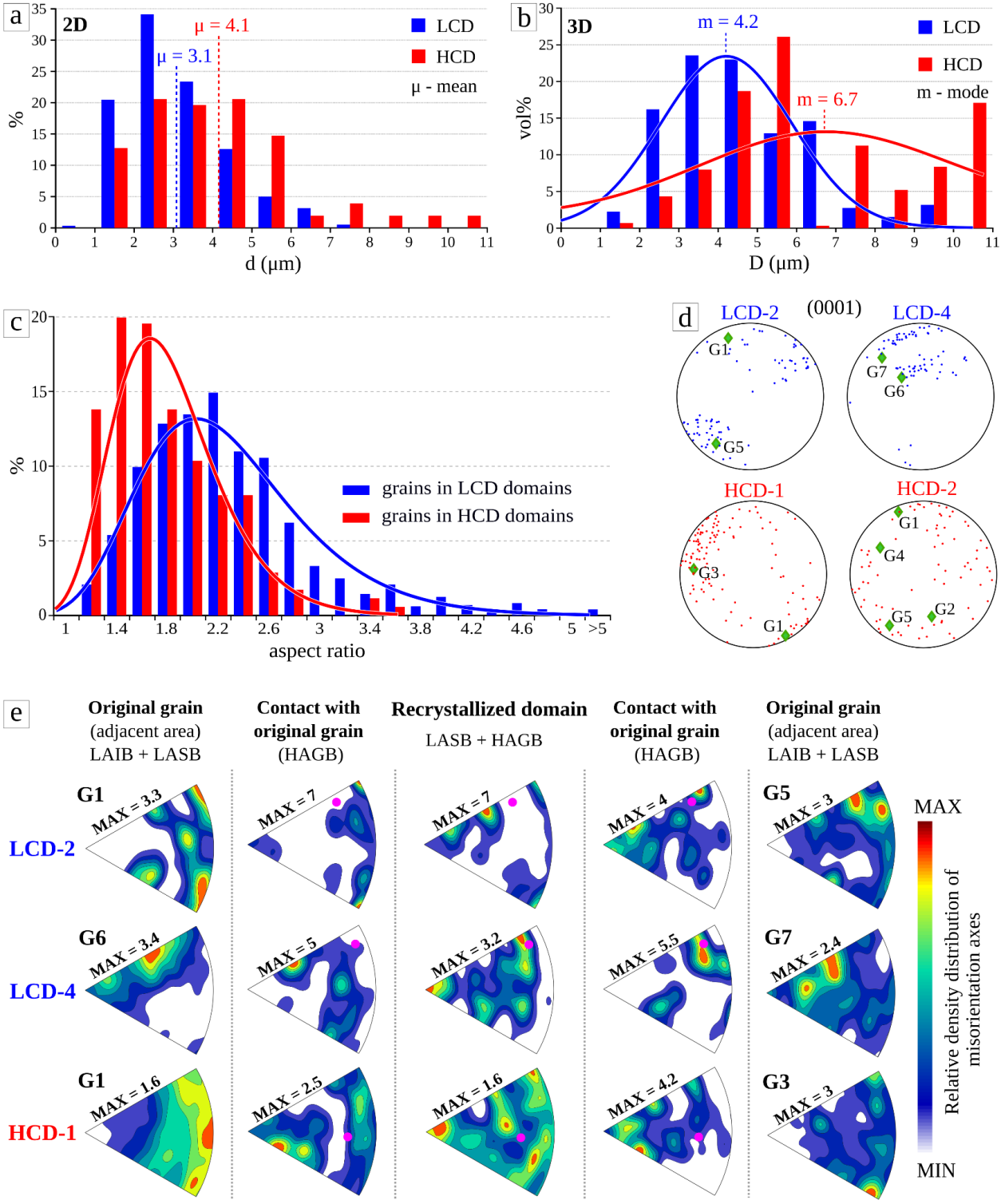

Figure 12. *Characteristics of LCD and HCD recrystallized domains presented in Figure 11c.* ***a-b)*** *Grain size distributions of recrystallized grains for LCD (blue) and HCD (red) domains; a) presented by numerical frequency (%) of equivalent diameters of 2D grain sections (d), with mean values (μ) marked by dashed lines; b) presented by volume percentage (vol%) of equivalent diameters of 3D grains (D), with Gaussian curve fits and mode values (m).* ***c)*** *Aspect ratios of the recrystallized grains in LCD and HCD domains, with log-normal density functions.* ***d)*** *Pole figures of (0001) showing crystallographic orientation of original grains (G1-G7 in Figure 11c; green diamonds) and neighboring recrystallized grains from LCD (blue dots) and HCD (red dots) domains.* ***e)*** *IPFs for -3m symmetry showing distribution of boundary misorientation axes from correlated misorientation across LAIB, LASB and HAGB boundaries in the LCD and HCD recrystallized domains, in the adjacent portions of the original grains G1-G7, and across the contact between the recrystallized and original grains; pink dots mark misorientation axis between the original grains. Contours in the IPFs correspond to density distribution of misorientation axes with their maximum determined for each inverse pole figure.*

3.7. Recrystallization in relation to added H_2O

The quantification of recrystallization together with the LCD/HCD distinction has been evaluated in the most deformed parts of the higher strain samples in the two as-is (568PP and 574PP) and two H_2O-added (567PP and 576PP) samples. The area of recrystallized regions was mapped (vectorized as polygons) and their distribution was inspected in the digitized maps. An example of the distribution of LCD and HCD domains is shown for as-is sample 568PP and H_2O-added sample 567PP in **Figure 13a** and **b**, respectively. The proportion of the recrystallized material determined from digitized maps of the four samples ranges between 15% and 19%, without systematic difference between the as-is and H_2O-added samples.

The LCD domains occupy a greater area (A) than the HCD domains in all four samples as demonstrated by the A_{LCD}/A_{HCD} ratio >1. The A_{LCD}/A_{HCD} ratio is much closer to 1 for H_2O-added samples (1.07 and 1.19 for 567PP and 576PP) than for as-is samples (1.83 and 2.19 for 568PP and 574PP). The differences in A_{LCD}/A_{HCD} ratios between as-is and H_2O-added samples document that the proportion of HCD recrystallization increases with the addition of H_2O.

The distribution and shape of digitized LCD and HCD domains show elongated LCD domains aligned parallel to long segments of grain boundaries and more equi-dimensional HCD domains at triple and quadruple junctions of the original grains. The rose diagrams in **Figure 13a-b** show a strong shape preferred orientation of LCD domains sub-perpendicular to the orientation of σ_1 principal stress (shortening direction). In contrast, the HCD domains show only weak to no shape preferred orientation. The diagrams in **Figure 13c** show considerably lower solidity of LCD domain polygons compared to the HCD domains, regardless of the aspect ratio of domains, while in case of HCD domains, solidity is generally increasing with the aspect ratio. The LCD domains, however, show much larger aspect ratios (up to 13) than HCD domains (up to 7). This demonstrates the invasiveness of LCD domains between the original grains, while the HCD domains are more compact and pore-like. The higher deltP and deltA values of LCD domains compared to the HCD (**Fig. 13d**) point to more complex, lobate and worm-like shapes of the LCD domains, as well as more rounded (convex) shapes of HCD domains.

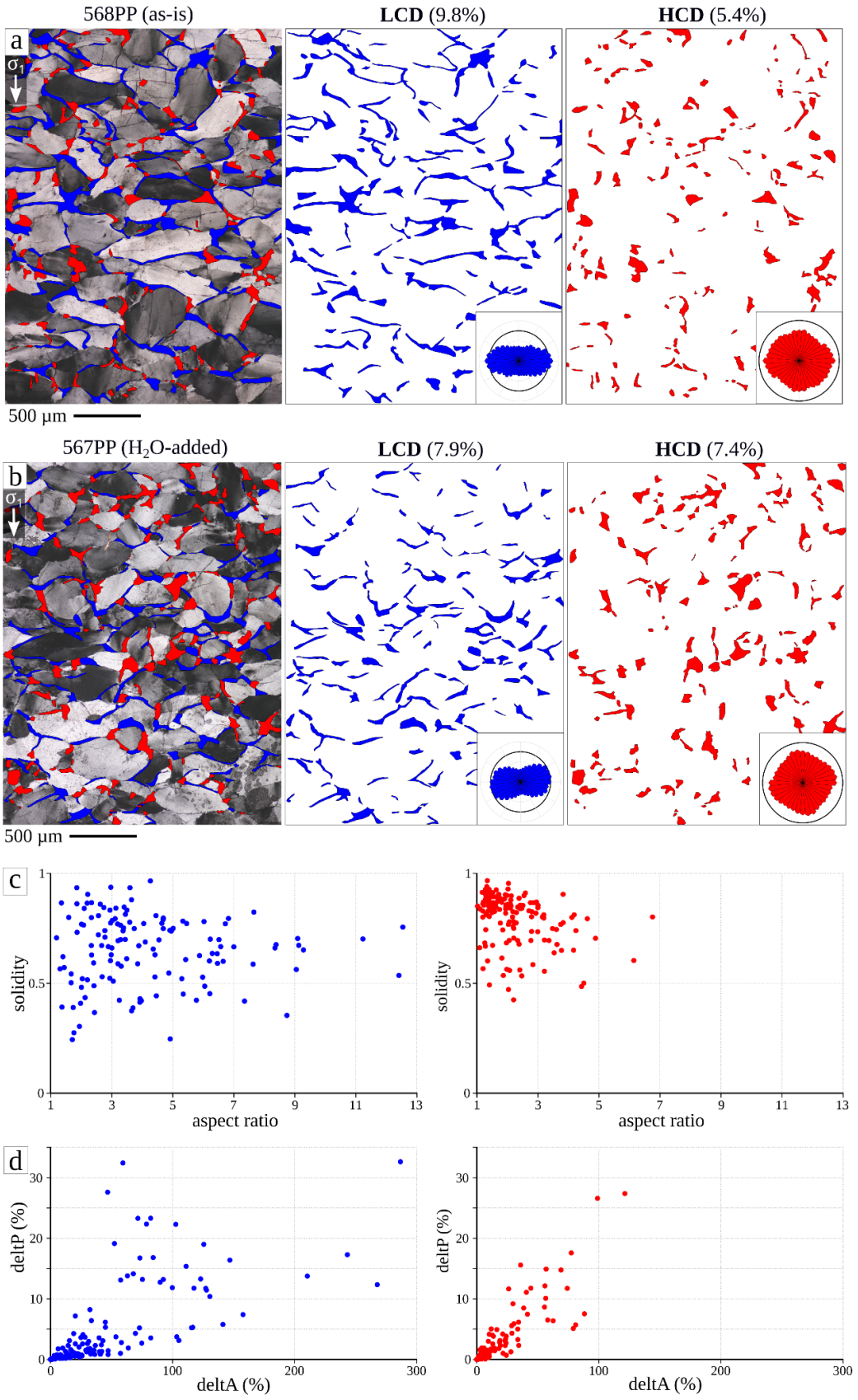

Figure 13. *Cross polarized micrographs and digitized maps of LCD (blue) and HCD (red) recrystallized domains covering the most deformed parts of* ***(a)*** *as-is sample 568PP and* ***(b)*** *H_2O-added sample 567PP. Rose diagrams in the bottom right corners of the digitized maps show orientation distribution of segmented domain boundaries with respect to the shortening direction, with the black circle marking proportion of 3%. The fractional volume is indicated above each map. Diagrams in* ***(c-d)*** *show (c) solidity with respect to the aspect ratio and (d) deltP versus deltA relationships of the LCD (blue) and HCD (red) domains. See text for definitions of solidity, deltP and deltA.*

4. Discussion

4.1. Recrystallization and reconstitution of the material

All higher strain samples show up to approximately 20% of recrystallized quartz, concentrated in the more deformed parts of the samples (**Figs. 7, 11**). A large fraction of the recrystallized material shows a change in luminescence color from yellow or cyan-blue (of the original sand grains) and dark brown (of the original cement) to blue (**Figs. 5, 6, 7, 8, 9**). Such changes in luminescence reflect the reconstitution of the quartz material, and are caused by different defects in the crystal structure of quartz, including the incorporation of trace elements (Ramseyer et al., 1988; Götze et al., 2001; Götze, 2012). Spear and Wark (2009) and Bestmann and Pennacchioni (2015) have inferred the blue luminescence to be caused by a Ti-exchange for Si. Since rutile is present as a potential Ti-source, this exchange may be possible, but no trace element analytics have been performed to confirm this in our samples. Raimbourg et al. (2015) and Molinero-Garcia et al. (2022) found increased concentrations of Al in the blue-luminescent quartz. Even though our results cannot confirm differences in Al-content (due to insufficient sensitivity of the analytics) in reconstituted and original quartz material (cf. **Fig. 14b-c**), incorporation of Al might also be possible (**Fig. 14c**). In either case, the trace element exchange in the quartz structure is demonstrated by the blue luminescence associated with defects at the 450 nm wavelength emission band, while defects related to the 650 nm wavelength emission band of the original sand grains and cement disappeared (**App. 3**). Similar changes in luminescence in deformed quartz have been described by Nègre et al. (2021) and interpreted as a result of trace element incorporation.

As diffusion of trace elements in quartz is slow even at the temperatures of our experiments (900°C; e.g., Cherniak et al., 2007), the change in luminescence during experiments (and in nature) cannot be produced by diffusion. It typically requires exchange with a fluid by grain boundary migration processes (Rusk et al., 2008; Grujic et al., 2011; Bestmann et al., 2015; Nachlas et al., 2018), even though equilibrium compositions may not always be produced by such a migration process (e.g., Hay and Evans, 1987; Negrini et al., 2014). In any case, as demonstrated by lobate grain boundaries associated with appearance of the blue luminescence (**Fig. 5b**), the observed blue luminescence can be used as a tracer for a H_2O-promoted reconstitution of quartz material by grain boundary migration, i.e., recrystallization *sensu lato*. Due to fluid migration through cracks, the reconstitution of material along the cracks makes them easily traceable in CL maps, even after they are healed (**Fig. 5c**).

Recrystallization that takes place during deformation (dynamic or syn-deformational recrystallization; Stunitz, 1998) is usually achieved by two principal mechanisms: Grain boundary migration (GBM) and progressive subgrain rotation (SGR) (e.g., Poirier and Guillope, 1979; Urai et al., 1986; Drury and Urai, 1990). The formation and progressive rotation of subgrains is an important nucleation mechanism for new grains in our samples. This is demonstrated by the misorientation analysis of low angle boundaries within original grains and low and high angle boundaries in domains of newly formed grains, particularly in the low crack density (LCD) regions (**Figs. 10e, 12e**). Dislocation glide in prism <a>, rhomb <a> and occasional basal <a> slip systems have been inferred for such misorientation relationships. The highest frequency of the c-axis as a misorientation axis is consistent with tilt boundaries of prism <a> slip, and, in addition, twist boundaries of the basal <a> slip (**Fig. 10b-c**; e.g., Kilian and Heilbronner, 2017). It is interesting to

see that subgrain boundaries formed in this way do not produce a change in luminescence, as seen in **Figure 11g**, where the high angle boundaries (black) are only present in the blue luminescent region, whereas the subgrain boundaries (red) occur in the region of dark cement that has not changed the luminescence. The same is observed for many internal low angle boundaries in original grains (green in **Fig. 11g**). Thus, the subgrain boundaries do not appear to migrate nor exchange with H_2O, and therefore do not change the CL signal.

When grain boundaries during their migration sweep whole grains, such a recrystallization is termed "grain boundary migration recrystallization" (Poirier and Guillope, 1979). If the process of GBM does not sweep whole grains but is restricted to the grain boundary region of the old grains (and eventually leading to their consumption), it is commonly termed "bulging recrystallization" (BLG; e.g., Stipp et al., 2002a,b). The operation of GBM in our samples is evident by the change in the CL signal in many recrystallized regions of the samples, and, more prominently in H_2O-added samples, it starts to operate at very low strains, as demonstrated by blue-luminescent lobate grain boundaries in **Fig. 5a-b**. Relatively small sizes of recrystallized grains (3D modes of ~4 to ~7 microns; **Fig. 12b**) indicate that the extent of GBM is very limited and the recrystallization observed here geometrically is considered as BLG. However, GBM itself does not produce new grains, it only modifies the grain size and shape after the grains are nucleated.

The larger part of observed recrystallized material shows a change in luminescence, and much of this material is clearly related to cracks (**Figs. 5a,c, 9** and **11a-f**). The nucleation of recrystallized grains by cracking has been described for natural quartz samples by van Daalen et al. (1999) and for experimental samples by Vernooij et al. (2006) and Stünitz et al. (2003; 2017). The higher crack density (HCD) regions often show a misorientation relationship that is not easily connected to a particular slip system in quartz by simple assumptions (only tilt or twist boundaries, etc.; **Figs. 10, 12**). Nevertheless, low and high angle boundaries without systematic misorientation relationships are common in such regions (**Figs. 10e** and **12e**). The cracks frequently show a mode I crack geometry as they are subparallel to the σ_1 orientation (**Figs. 5c** and **7c**). Even though such "axial splitting" cracks typically tend to form at low confining pressures (e.g., during attaining the desired P-T conditions), the CL image of hot pressed sample in **Appendix 4** does not document these features. Therefore, it is inferred that the cracking must have occurred later, during the loading stage of experiments. Other cracks can have other orientations and may have formed during the main deformation. The formation of new grains in cracked regions demonstrates that small fragments have been nuclei of new grains (e.g., **Figs. 5c, 6, 8e-f** and **9a**). The fragment boundaries are inferred to have been mobile, so that local grain boundary migration has led to grain growth and an exchange of trace elements in these new grains. The fact that some fragments have rounded grain shapes is consistent with the activity of local GBM (**Figs. 11** and **12c**).

Summarizing, it is found that newly recrystallized grains nucleate by two different mechanisms: (1) progressive subgrain rotation (SGR) and (2) cracking. The low crack density (LCD) regions correspond to the SGR-dominated processes, whereas the high crack density regions (HCD) correspond more to the crack related fragmentation (**Fig. 12**). This is documented by the grain size produced by cracking, which tends to be more variable and partially larger than that produced by SGR (**Figs. 11c** and **12a-b**). In addition, the aspect ratios of new grains produced by SGR tend to be bigger (**Figs. 11g** and **12c**). It is assumed that with increasing strain and continuing GBM, these differences will be attenuated or disappear.

4.2. Cracking

All samples are deformed at low differential stresses (~20% of P_{conf}), far below the Goetze criterion ($\Delta\sigma \leq P_{conf}$), where plastic deformation typically dominates over brittle mechanisms (Kohlstedt et al., 1995). The same situation has been observed in a recent study by Nègre et al. (2021), where 0.1 wt% of H_2O had been added to the same sample material. Here, in addition to 0.1 wt% H_2O-added, as-is (oven dried at 115°C) samples have been also used, where H_2O contents will be lower. Thus, the potential effect of pore pressure on the Goetze criterion is expected to be lower in as-is samples, too. Using a similar experimental setup, Nègre et al. (2021) have determined that >90% of the sample strain is accommodated by crystal plastic deformation of the original quartz grains. In addition, the cracks do not show observable offsets, so they do not contribute significantly to the sample strain. However, our low strain samples have shown that formation of crack and microcrack networks helps to redistribute H_2O within the samples at the early stages of deformation, i.e. before observable dynamic recrystallization, which was observed also by Trepmann and Stöckhert (2003).

The HCD regions show an isotropic orientation in the samples, in contrast to the LCD regions (**Fig. 13**). Some of the HCD regions show faceted overgrowth rims on recrystallized grains, as well as porosity and amorphous material traced by high relative Al-contents (**Figs. 8, 9** and **14**). The amorphous material is interpreted as a quenched melt that formed due to breakdown of hydrous impurities (phyllosilicates), in the presence of H_2O and SiO_2. The porosity refers to bubbles that have most likely been occupied by exsolved vapor phase from cooling of the fluid/melt phase during the quenching of the experiments (brown arrows in **Fig. 8e**). The faceted overgrowths are observed on crack-related nuclei in melt/fluid-filled pockets and cracks (**Fig. 9**). These features have also been observed in other quartz experiments by Palazzin et al. (2018) and Schmocker et al. (2003). Fluid pockets mainly appear in association with cracks, oriented at a low angle to the σ_1 direction and do not coalesce in the samples (**Fig. 7c**). These structures are consistent with the melt distribution at very low percentages demonstrated by Dell'Angelo and Tullis (1988), Rutter and Neumann (1995) and Menegon et al. (2011). There are three reasons that indicate that the cracks did not have much effect on the strength of the samples: (1) their nature as mode I cracks, (2) their lack of offset and coalescence and (3) their low total volume fractions. Instead of producing strain by brittle deformation, the deformation is clearly dominated by crystal plasticity. Open cracks thus serve as fluid-storage, and the segregated fluid phase does not seem to affect crack propagation significantly. Considering its low volume fraction (~1%), it is likely that the fluid does not significantly wet the grain boundaries, which is consistent with the relatively high viscosity of such SiO_2-rich and H_2O-poor melts. Menegon et al. (2011) reported that melt located in isolated pockets, with volume fraction of ~5%, does not control mechanical behavior of their samples. However, their samples taken from the melt-depleted areas showed higher mechanical strengths.

The LCD recrystallized regions dominated by SGR are preferentially oriented sub-perpendicular to the σ_1 direction, whereas the HCD regions are more randomly oriented and located at triple junctions (**Fig. 13a-b**). The shape anisotropy of HCD domains is very low, whereas it is high for LCD regions (**Fig. 13c-d**). These features support the interpretation that the cracks tend to form as mode I cracks and cause recrystallization mainly at the triple junctions, whereas the SGR recrystallization develops in plastically deformed regions, predominantly at high stress sites (grain boundaries), normal to σ_1.

4.3. H_2O and strength of samples

Although the average flow stress of H_2O-added samples is ~30 MPa lower (at 15-30% strain) than that of the as-is samples (**Fig. 1a**), this difference is still within the ± 30 MPa error range given by Holyoke and Kronenberg (2010). All samples tend to weaken slightly after 15-20% strain (**Fig. 1a**). The conditions of deformation correspond to those of regime 2 of Hirth and Tullis (1992), which is generally defined by medium yield stresses (about 200-300 MPa), minor strain softening and recrystallization governed by subgrain rotation, as a recovery mechanism during dislocation glide. Kronenberg and Tullis (1984) have documented a lower strength of samples with smaller grain size in H_2O-added samples. We have observed excess H_2O in the form of small fluid/melt pockets, so that the H_2O contents of our samples are inferred to correspond to those of H_2O-added samples of Kronenberg and Tullis (1984). We interpret the weakening of our samples after 15-20% strain as a consequence of an increased amount of fine grained recrystallized material in our samples with increasing strain (cf. Nègre et al., 2021; **Figs. 1a, 7c**).

The stress exponents determined from strain rate stepping experiments range from n=1.45 to n=2.13 (**Table 2**, **Fig. 2**). It is important to note that the lowest value of 1.45 has the largest statistical error (lowest R^2 values), so that the upper range of values appears more reliable. In addition, it should be pointed out that correction for stress in salt assemblies reported by *Holyoke and Kronenberg (2010),* not applied to our experimental data, would further reduce the n-values in **Figure 2**. N-values in the range of $n\approx2$ have been determined by Luan and Paterson (1992) (for gel-origin-samples), Jaoul et al. (1984), Fukuda et al. (2018) and Richter et al. (2018), consistent with the range of 1 GPa experiments given here, but n-values in the range of 3 to 4 are commonly used in flow laws describing dislocation creep in quartz (Paterson and Luan, 1990; Gleason and Tullis, 1995; Hirth et al., 2001; Rutter and Brodie, 2004a,b; Tokle et al., 2019; Lu and Jiang, 2019; Lusk et al., 2021). N-values of 3-5 are typical for climb-controlled dislocation creep (e.g., Karato, 2008; Paterson, 2013). Since our stress exponents of $n\approx2$ do not fall in this range, either dislocation creep is not climb-controlled in our samples, or other deformation mechanisms operate in parallel, and may be rate-limiting. As the bulk sample strain is dominantly accommodated by crystal plasticity of original quartz grains, it is inferred that another deformation or recovery process has operated in parallel with dislocation glide. Nègre et al. (2021) have argued for grain boundary processes by dissolution-precipitation to operate together with dislocation glide/creep. Since the H_2O promoted GBM is also included in such grain boundary processes, as documented in recrystallization microstructures of our low strain H_2O-added sample (**Fig. 5b**), we therefore infer dissolution-precipitation-creep (DPC), most likely together with grain boundary sliding, to operate in combination with dislocation processes in our samples. The increased solubility of SiO_2 at elevated temperatures and pressures (Manning, 1994, 2018) makes such a mechanism very efficient at our experimental conditions. A local stress drop leads to oversaturation of the fluid and thus to precipitation in such low stress areas during DPC. The DPC and grain boundary sliding processes may act in the grain boundary regions to accommodate for an insufficient number of active slip systems during dislocation glide, similar to processes in “wet” ice (Kuiper, 2020; Goldsby and Kohlstedt, 2001). In ice, the basal glide is accommodated by grain boundary sliding resulting in n-values between 1.8 and 2.4 over some large range of grain sizes (Goldsby and Kohlstedt, 2001).

The combination of dislocation creep, DPC and grain boundary sliding as an accommodation at grain boundaries may result in a stress exponent of $n \leq 2$ (**Fig. 2**).

Despite lower reliability of the *n*-value of 1.45, the *n*-values for higher confining pressure are lower (for as-is and H_2O-added samples) than those at lower confining pressure (1.45-1.77 at 1.5 GPa and 1.94-2.13 at 1 GPa, respectively). This appears to be consistent with a greater activity of DPC processes at higher pressure, so that these processes become more important and are expected to lower the *n*-values. The fact that as-is samples tend to show lower *n*-values than the H_2O-added samples (**Table 2**) is not readily explained by similar arguments as the higher H_2O contents do not necessarily lead to increased activity of DPC. In our case the H_2O-added samples show higher amounts of crack-related recrystallization and melt/fluid pockets which may reduce the level of H_2O saturation along grain boundaries. In addition, the exact nature of DPC is rather complex, since it necessarily involves grain boundary sliding processes, which is difficult to demonstrate even in experimentally deformed samples. These differences in *n*-values thus could simply be the result of errors, which originate from the sensitivity of the external load cell giving the potential error in differential stress record within +/- 30 MPa (Holyoke and Kronenberg, 2010).

The lower strength of H_2O-added samples may be associated with an increased activity of DPC processes. This is suggested by the microstructures of the low strain samples where the weaker H_2O-added sample shows clear evidence for H_2O-promoted GBM, while the stronger as-is sample shows only minor cracking (cf. **Figs. 4** and **5**). In addition, in the higher strain samples, cracking as a consequence of increased pore pressure could lead to enhancement of the DPC processes. The pore pressure at the high pressures of the experiments and low porosity has been considered to be close to $P_{fluid} = P_{lithostatic}$ (e.g., Hirth and Beeler, 2015; Beeler et al., 2016). At this condition, cracking may occur, even at higher confining pressures, as it is demonstrated in our study. However, the isolated geometry of the fluid/melt pockets and their lack of offset indicate that cracks themselves do not contribute as a strain-producing agent during deformation. Cracks never coalesce and never form through-going fractures in any of the samples. For this reason, cracking is not inferred to control the sample strength significantly, although it contributes to increasing proportion of the recrystallized material and enhancement of the DPC process.

4.4. Comparison with quartz recrystallization in nature

Dynamic recrystallization of quartz in natural samples is commonly used as evidence for dislocation creep deformation mechanism operating (typically at elevated temperatures) in the viscously deforming parts of crust. Even though viscous deformation may be dominant, crack-related recrystallization of deep-seated crustal rocks has been unequivocally demonstrated in a number of recent studies (e.g., FitzGerald and Stunitz 1993 and references therein). Some of these studies argued for brittle failure associated with high stresses relaxed by a seismic event and post-seismic viscous creep (Trepmann et al., 2007; Trepmann and Stöckhert, 2013; Okudaira et al., 2015; Bukovská et al., 2016; Menegon et al., 2017) while others associated cracking with lower stresses typical for viscous creep of the lower crust (Stünitz and Fitz Gerald 1993; Vernooij et al., 2006; Menegon et al., 2013; Stünitz et al., 2017). For quartz, the latter has been demonstrated in this study and few other experimental studies (Fitz Gerald et al. 1991; Vernooij et al., 2006; Négre et al., 2021), implying the possibility for simultaneous cracking and dislocation creep.

Recrystallization of quartz due to simultaneous (or initial) cracking and subgrain rotation concluded in this study shows microstructures (**Fig. 14a**) that are extremely similar to those reported from nature (e.g. Stipp et al., 2002b; Jeřábek et al., 2007) or other experimental studies concluding that only dislocation creep had operated (Hirth and Tullis 1992; Stipp and Tullis, 2003). At the same time, cracking and cracked fragments (orange arrows in **Fig. 14a-b**) are unlikely to be recognized easily in natural samples. One of the reasons for this is the ubiquitous presence of H_2O in natural samples that enhances grain boundary mobility and dissolution-precipitation processes. Grain boundary mobility will result in continuous erasing of brittle features as documented in our study (e.g., **Fig. 5a,c**). Indeed, a major portion of recrystallized grains in our samples, nucleated either by cracking or subgrain rotation, show material reconstitution by GBM related to dissolution-precipitation processes, as demonstrated by the change in luminescence (e.g., **Figs. 5a-b, 6b**). In this respect, it is interesting to point out that the grain size of both types of recrystallized grains (**Fig. 12a-b**) is nearly identical, despite differences in nucleation processes, and consistent with piezometric relations for dislocation creep in quartz (Stipp and Tullis 2003). Consequently, the only way to recognize the concurrent brittle mechanism for nucleation in dynamic recrystallization of quartz would be the detection of healed cracks crosscutting the original grains. These are easily recognized in our samples as they are marked by the blue luminescence resulting from our experimental conditions. Since the observed healed cracks show no significant offset, they usually appear as low angle boundaries in the EBSD maps (e.g., **Figs. 5d** and **8c**), which show no systematic relationship to quartz slip systems. In natural samples, however, the healed cracks will not be recognized by luminescence (e.g. Raimbourg et al., 2015), except in weakly deformed and metamorphosed quartz. In addition, the crack-related low angle boundaries may easily be confused with subgrain boundaries. The evidence for cracking in dynamically recrystallized natural samples is reflected by fluid inclusion trails, sometimes preserved in the relict original grains (e.g. Boullier 1999; Faleiros et al., 2010; Hirth and Beeler, 2015). The question arises if a connection between inclusion trails and dynamic recrystallization of quartz can be established in future studies on quartz natural deformation. Summarizing, it appears very likely that recrystallization of quartz in nature partly involves cracking in a nucleation stage, as shown in our experiments.

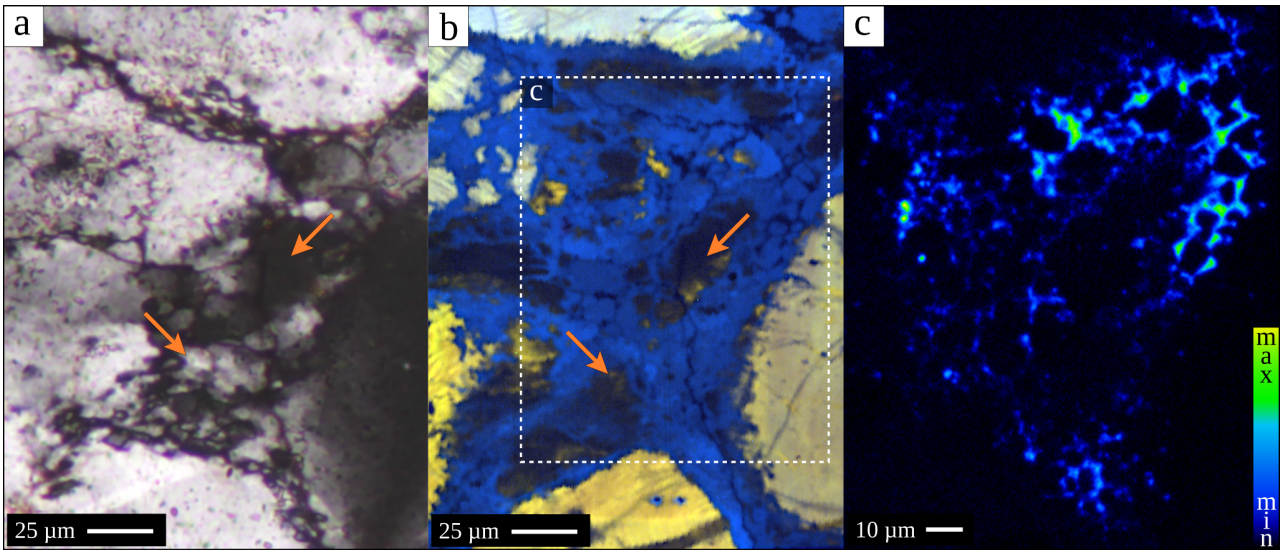

Figure 14. *Comparison of* ***(a)*** *cross polarized and* ***(b)*** *CL image of a recrystallized domain, showing cracked fragments (orange arrows) overprinted by blue luminescent reconstituted material.* ***c)*** *Al-map demonstrates the increased Al-concentration overlapping only with the fluid channels and pockets, while the difference in Al-content between reconstituted and original quartz material is not detectable.*

5. Conclusions

Deformation experiments on as-is and H_2O-added quartzite samples show mechanical strengths in the range of 154-227 MPa, with slightly weaker average strength of H_2O-added samples, and stress exponent values between 1.94-2.13 for 1 GPa experiments and 1.45-1.77 for 1.5 GPa experiments.

Sample strain was accommodated dominantly by crystal plasticity, consistent with the low stresses of the deformation. In parallel with plasticity, cracking occurred but has not produced significant sample strain.

Recrystallization of the original grains resulted from two nucleation processes: progressive subgrain rotation and cracking.

In the recrystallized domains, up to 20% of the material was reconstituted by grain boundary migration, as revealed by the change in luminescence to blue color. The material reconstitution appears to be facilitated by an aqueous environment (fluid pockets and channels).

Reconstitution of quartz occurred along healed cracks and high angle grain boundaries suggesting H_2O promoted grain boundary migration and dissolution-precipitation processes. The low angle boundaries do not migrate and thus preserve their original luminescence.

Stress exponent values around 2 are inconsistent with deformation by climb accommodated dislocation creep. Instead, we infer that dissolution-precipitation creep and grain boundary sliding occur as accommodation processes in the grain boundary regions simultaneously with dislocation glide, similar to “wet” ice deformation.

Observed with cross polarized light, many recrystallized domains formed by cracking and fragmentation could mistakenly be attributed to SGR-dominated recrystallization. Detailed microstructural analyses by CL, BSE, EMPA and EBSD reveal a variety of recrystallized regions

with new grains of different origin, and low crack density (LCD) and high crack density (HCD) domains being two endmembers in a range. SGR processes appear to be the dominant nucleation mechanism only in the LCD domains, while fragmentation due to cracking takes place mostly in HCD zones.

Compared to as-is samples, the H_2O-added samples reveal a higher proportion of crack related recrystallized material.

Replacement of material by grain boundary migration and dissolution-precipitation at high angle boundaries produced by cracking at lower strains will make the detection of a crack origin difficult or even impossible at higher strains (e.g., in nature). Nevertheless, new grains produced by recrystallization in nature may partially nucleate by crack-related processes as demonstrated in our experiments.

Acknowledgments:
We would like to acknowledge financial support from the Grant Agency of Charles University (GAUK 488119) and the Center of Geosphere Dynamics (UNCE/SCI/006). We thank Rune Stien and Raoul Heilbronner for the assistance during the material sampling within the ELKEM quarry in the Austertana region. Rüdiger Kilian and Jacques Précigout are thanked for helpful discussions and suggestions. A. Kronenberg and an anonymous reviewer are thanked for useful suggestions to improve the manuscript and V. Toy is thanked for editorial handling.

References:

Bachmann, F., Hielscher, R., Schaeben, H., 2011. Grain detection from 2d and 3d EBSD data-Specification of the MTEX algorithm. Ultramicroscopy 111. https://doi.org/10.1016/j.ultramic.2011.08.002

Bailey J.E., Hirsch, P.B., 1962. The recrystallization process in some polycrystalline metals. Proceedings of the Royal Society of London. Series A. Mathematical and Physical Sciences 267, 11–30. https://doi.org/10.1098/rspa.1962.0080

Bakker, R.J., Jansen, J.B.H., 1990. Preferential water leakage from fluid inclusions by means of mobile dislocations. Nature 345. https://doi.org/10.1038/345058a0

Beeler, N.M., Hirth, G., Thomas, A., Bürgmann, R., 2016. Effective stress, friction, and deep crustal faulting. Journal of Geophysical Research: Solid Earth 121. https://doi.org/10.1002/2015JB012115

Bestmann, M., Pennacchioni, G., 2015. Ti distribution in quartz across a heterogeneous shear zone within a granodiorite: The effect of deformation mechanism and strain on Ti resetting. Lithos 227. https://doi.org/10.1016/j.lithos.2015.03.009

Blacic, J.D., 1975. Plastic-deformation mechanisms in quartz: The effect of water. Tectonophysics 27. https://doi.org/10.1016/0040-1951(75)90021-9

Blacic, J.D., Christie, J.M., 1984. Plasticity and hydrolytic weakening of quartz single crystals. Journal of Geophysical Research. https://doi.org/10.1029/jb089ib06p04223

Bouchez, J.L., Pecher, A., 1981. The Himalayan Main Central Thrust pile and its quartz-rich tectonites in central Nepal. Tectonophysics 78. https://doi.org/10.1016/0040-1951(81)90004-4

Boullier, A.M., 1999. Fluid inclusions: Tectonic indicators. Journal of Structural Geology 21. https://doi.org/10.1016/S0191-8141(99)00039-5

Brace, W.F., Kohlstedt, D.L., 1980. Limits on lithospheric stress imposed by laboratory experiments. Journal of Geophysical Research: Solid Earth 85. https://doi.org/10.1029/jb085ib11p06248

Bukovská, Z., Jeřábek, P., Morales, L.F.G., 2016. Major softening at brittle-ductile transition due to interplay between chemical and deformation processes: An insight from evolution of shear bands in the South Armorican Shear Zone. Journal of Geophysical Research: Solid Earth 121. https://doi.org/10.1002/2015JB012319

Cherniak, D.J., Watson, E.B., Wark, D.A., 2007. Ti diffusion in quartz. Chemical Geology 236. https://doi.org/10.1016/j.chemgeo.2006.09.001

Cordier, P., Doukhan, J.C., Ramboz, C., 1994. Influence of dislocations on water leakage from fluid inclusions in quartz: a quantitative reappraisal. European Journal of Mineralogy 6, 745–752. https://doi.org/10.1127/ejm/6/6/0745

Dell'Angelo, L.N., Tullis, J., 1988. Experimental deformation of partially melted granitic aggregates. Journal of Metamorphic Geology 6, 495–515. https://doi.org/10.1111/j.1525-1314.1988.tb00436.x

Dell'Angelo, L.N., Tullis, J., 1989. Fabric development in experimentally sheared quartzites. Tectonophysics 169, 1–21. https://doi.org/10.1016/0040-1951(89)90180-7

Den Brok, S.W.J., Spiers, C.J., 1991. Experimental evidence for water weakening of quartzite by microcracking plus solution-precipitation creep. Journal of the Geological Society 148, 541–548. https://doi.org/10.1144/gsjgs.148.3.0541

Doukhan, J.C., 1995. Lattice Defects and Mechanical Behaviour of Quartz SiO 2. Journal de Physique III 5. https://doi.org/10.1051/jp3:1995228

Drury, M.R., Urai, J.L., 1990. Deformation-related recrystallization processes. Tectonophysics 172, 235–253. https://doi.org/10.1016/0040-1951(90)90033-5

Faleiros, F.M., Campanha, G.A. da C., Bello, R.M. da S., Fuzikawa, K., 2010. Quartz recrystallization regimes, c-axis texture transitions and fluid inclusion reequilibration in a prograde greenschist to amphibolite facies mylonite zone (Ribeira Shear Zone, SE Brazil). Tectonophysics 485, 193–214. https://doi.org/10.1016/j.tecto.2009.12.014

Fitz Gerald, J.D., Boland, J.N., McLaren, A.C., Ord, A., Hobbs, B.E., 1991. Microstructures in water-weakened single crystals of quartz. Journal of Geophysical Research 96, 2139–2155. https://doi.org/10.1029/90jb02190

Fitz Gerald, J.D., Stünitz, H., 1993. Deformation of granitoids at low metamorphic grade. I: Reactions and grain size reduction. Tectonophysics 221. https://doi.org/10.1016/0040-1951(93)90163-E

Fukuda, J., Holyoke, C.W., Kronenberg, A.K., 2018. Deformation of Fine-Grained Quartz Aggregates by Mixed Diffusion and Dislocation Creep. Journal of Geophysical Research: Solid Earth 123, 4676–4696. https://doi.org/10.1029/2017JB015133

Gerretsen, J., Paterson, M.S., McLaren, A.C., 1989. The uptake and solubility of water in quartz at elevated pressure and temperature. Physics and Chemistry of Minerals 16. https://doi.org/10.1007/BF00199553

Gleason, G.C., Tullis, J., 1995. A flow law for dislocation creep of quartz aggregates determined with the molten salt cell. Tectonophysics 247, 1–23. https://doi.org/10.1016/0040-1951(95)00011-B

Gleason, G.C., Tullis, J., Heidelbach, F., 1993. The role of dynamic recrystallization in the development of lattice preferred orientations in experimentally deformed quartz aggregates. Journal of Structural Geology 15, 1145–1168. https://doi.org/10.1016/0191-8141(93)90161-3

Goldsby, D.L., Kohlstedt, D.L., 2001. Superplastic deformation of ice: Experimental observations. Journal of Geophysical Research: Solid Earth 106. https://doi.org/10.1029/2000jb900336

Götze, J., Plötze, M., Habermann, D., 2001. Origin, spectral characteristics and practical applications of the cathodoluminescence (CL) of quartz - A review. Mineralogy and Petrology 71, 225–250. https://doi.org/10.1007/s007100170040

Götze, J., 2012. Application of cathodoluminescence microscopy and spectroscopy in geosciences. Microscopy and Microanalysis. 1270–1284. https://doi.org/10.1017/S1431927612001122

Griggs, D.T., Blacic, J.D., 1965. Quartz: Anomalous weakness of synthetic crystals. Science 147, 292–295. https://doi.org/10.1126/science.147.3655.292

Griggs, D., 1967. Hydrolytic Weakening of Quartz and Other Silicates. Geophysical Journal of the Royal Astronomical Society 14. https://doi.org/10.1111/j.1365-246X.1967.tb06218.x

Griggs, D., 1974. A model of hydrolytic weakening in quartz. Journal of Geophysical Research 79. https://doi.org/10.1029/jb079i011p01653

Grujic, D., Stipp, M., Wooden, J.L., 2011. Thermometry of quartz mylonites: Importance of dynamic recrystallization on Ti-in-quartz reequilibration. Geochemistry, Geophysics, Geosystems 12. https://doi.org/10.1029/2010GC003368

Guillope, M., Poirier, J.P., 1980. A model for stress-induced migration of tilt grain boundaries in crystals of NaCl structure. Acta Metallurgica 28. https://doi.org/10.1016/0001-6160(80)90065-6

Hay, R.S., Evans, B., 1987. Chemically induced grain boundary migration in calcite: temperature dependence, phenomenology, and possible applications to geologic systems. Contributions to Mineralogy and Petrology 97. https://doi.org/10.1007/BF00375220

Heilbronner, R., Barrett, S., 2014. Image analysis in earth sciences: Microstructures and textures of earth materials. Image Analysis in Earth Sciences: Microstructures and Textures of Earth Materials. Springer. https://doi.org/10.1007/978-3-642-10343-8

Heilbronner, R., Bruhn, D., 1998. The influence of three-dimensional grain size distributions on the rheology of polyphase rocks. Journal of Structural Geology 20. https://doi.org/10.1016/S0191-8141(98)00010-8

Heilbronner, R., Keulen, N., 2006. Grain size and grain shape analysis of fault rocks. Tectonophysics 427. https://doi.org/10.1016/j.tecto.2006.05.020

Heilbronner, R., Kilian, R., 2017. The grain size(s) of Black Hills Quartzite deformed in the dislocation creep regime. Solid Earth 8. https://doi.org/10.5194/se-8-1071-2017

Hielscher, R., Schaeben, H., 2008. A novel pole figure inversion method: Specification of the MTEX algorithm. Journal of Applied Crystallography 41. https://doi.org/10.1107/S0021889808030112

Hirth, G., Teyssier, C., Dunlap, W.J., 2001. An evaluation of quartzite flow laws based on comparisons between experimentally and naturally deformed rocks. International Journal of Earth Sciences 90. https://doi.org/10.1007/s005310000152

Hirth, G., Beeler, N.M., 2015. The role of fluid pressure on frictional behavior at the base of the seismogenic zone. Geology 43. https://doi.org/10.1130/G36361.1

Hirth, G., Tullis, J., 1992. Dislocation creep regimes in quartz aggregates. Journal of Structural Geology 14. https://doi.org/10.1016/0191-8141(92)90053-Y

Holyoke, C.W., Kronenberg, A.K., 2010. Accurate differential stress measurement using the molten salt cell and solid salt assemblies in the Griggs apparatus with applications to strength, piezometers and rheology. Tectonophysics 494. https://doi.org/10.1016/j.tecto.2010.08.001

Jaoul, O., Tullis, J., Kronenberg, A., 1984. Effect of varying water contents on the creep behavior of heavitree quartzite. Journal of Geophysical Research. https://doi.org/10.1029/jb089ib06p04298

Jeřábek, P., Stünitz, H., Heilbronner, R., Lexa, O., Schulmann, K., 2007. Microstructural-deformation record of an orogen-parallel extension in the Vepor Unit, West Carpathians. Journal of Structural Geology 29. https://doi.org/10.1016/j.jsg.2007.09.002

Johnson, H.D., Levell, B.K., Siedlecki, S., 1978. Late Precambrian sedimentary rocks in East Finnmark, north Norway and their relationship to the Trollfjord-Komagelv fault. Journal of the Geological Society 135, 517–533. https://doi.org/10.1144/gsjgs.135.5.0517

Karato, S.I., 2008. Deformation of earth materials: An introduction to the rheology of solid earth, Deformation of Earth Materials: An Introduction to the Rheology of Solid Earth. https://doi.org/10.1017/CBO9780511804892

Kekulawala, K.R.S.S., Paterson, M.S., Boland, J.N., 2013. An Experimental Study of the Role of Water in Quartz Deformation. Geophysical Monograph Series. 49–60. https://doi.org/10.1029/gm024p0049

Kilian, R., Heilbronner, R., 2017. Analysis of crystallographic preferred orientations of experimentally deformed Black Hills Quartzite. Solid Earth 8, 1095–1117. https://doi.org/10.5194/se-8-1095-2017

Kohlstedt, D.L., Evans, B., Mackwell, S.J., 1995. Strength of the lithosphere: constraints imposed by laboratory experiments. Journal of Geophysical Research 100. https://doi.org/10.1029/95jb01460

Kronenberg, A.K., Kirby, S.H., Aines, R.D., Rossman, G.R., 1986. Solubility and diffusional uptake of hydrogen in quartz at high water pressures: Implications for hydrolytic weakening. Journal of Geophysical Research: Solid Earth 91, 12723–12741. https://doi.org/10.1029/jb091ib12p12723

Kronenberg, A.K., Tullis, J., 1984. Flow strengths of quartz aggregates: grain size and pressure effects due to hydrolytic weakening. Journal of Geophysical Research. https://doi.org/10.1029/jb089ib06p04281

Kuiper, E.J.N., De Bresser, J.H.P., Drury, M.R., Eichler, J., Pennock, G.M., Weikusat, I., 2020. Using a composite flow law to model deformation in the NEEM deep ice core, Greenland-Part 2: The role of grain size and premelting on ice deformation at high homologous temperature. Cryosphere 14. https://doi.org/10.5194/tc-14-2449-2020

Law, R.D., Schmid, S.M., Wheeler, J., 1990. Simple shear deformation and quartz crystallographic fabrics: a possible natural example from the Torridon area of NW Scotland. Journal of Structural Geology 12, 29–45. https://doi.org/10.1016/0191-8141(90)90046-2

Lexa, O., 2003. Numerical approach in structural and microstructural analyses. PhD thesis. Charles University, Prague.

Lu, L.X., Jiang, D., 2019. Quartz Flow Law Revisited: The Significance of Pressure Dependence of the Activation Enthalpy. Journal of Geophysical Research: Solid Earth 124, 241–256. https://doi.org/10.1029/2018JB016226

Luan, F.C., Paterson, M.S., 1992. Preparation and deformation of synthetic aggregates of quartz. Journal of Geophysical Research 97, 301–320. https://doi.org/10.1029/91JB01748

Lusk, A.D.J., Platt, J.P., Platt, J.A., 2021. Natural and Experimental Constraints on a Flow Law for Dislocation-Dominated Creep in Wet Quartz. Journal of Geophysical Research: Solid Earth 126. https://doi.org/10.1029/2020JB021302

Manning, C.E., 1994. The solubility of quartz in H_2O in the lower crust and upper mantle. Geochimica et Cosmochimica Acta 58. https://doi.org/10.1016/0016-7037(94)90214-3

Manning, C.E., 2018. Fluids of the Lower Crust: Deep Is Different., Annual Review of Earth and Planetary Sciences. https://doi.org/10.1146/annurev-earth-060614-105224

McLaren, A.C., Fitz Gerald, J.D., Gerretsen, J., 1989. Dislocation nucleation and multiplication in synthetic quartz: Relevance to water weakening. Physics and Chemistry of Minerals 16. https://doi.org/10.1007/BF00197016

McLaren, A.C., Retchford, J.A., 1969. Transmission Electron Microscope Study of the Dislocations in Plastically Deformed Synthetic Quartz. Physica Status Solidi (B) 33. https://doi.org/10.1002/pssb.19690330220

Menegon, L., Pennacchioni, G., Malaspina, N., Harris, K., Wood, E., 2017. Earthquakes as Precursors of Ductile Shear Zones in the Dry and Strong Lower Crust. Geochemistry, Geophysics, Geosystems 18. https://doi.org/10.1002/2017GC007189

Menegon, L., Nasipuri, P., Stünitz, H., Behrens, H., Ravna, E., 2011. Dry and strong quartz during deformation of the lower crust in the presence of melt. Journal of Geophysical Research: Solid Earth 116. https://doi.org/10.1029/2011JB008371

Menegon, L., Stünitz, H., Nasipuri, P., Heilbronner, R., Svahnberg, H., 2013. Transition from fracturing to viscous flow in granulite facies perthitic feldspar (Lofoten, Norway). Journal of Structural Geology 48. https://doi.org/10.1016/j.jsg.2012.12.004

Morrison-Smith, D.J., Paterson, M.S., Hobbs, B.E., 1976. An electron microscope study of plastic deformation in single crystals of synthetic quartz. Tectonophysics 33. https://doi.org/10.1016/0040-1951(76)90051-2

Molinero-García, A., Müller, A., Martín-García, J.M., Simonsen, S.L., Delgado, R., (2022). Provenance of quartz grains from soils over Quaternary terraces along the Guadalquivir River, Spain. Geoderma. 414, 115769. https://doi.org/10.1016/j.geoderma.2022.115769

Nachlas, W.O., Thomas, J.B., Hirth, G., 2018. TitaniQ deformed: Experimental deformation of out-of-equilibrium quartz porphyroclasts. Journal of Structural Geology 116. https://doi.org/10.1016/j.jsg.2018.07.012

Nègre, L., Stünitz, H., Raimbourg, H., Lee, A., Précigout, J., Pongrac, P., Jeřábek, P., 2021. Effect of pressure on the deformation of quartz aggregates in the presence of H_2O. Journal of Structural Geology 148. https://doi.org/10.1016/j.jsg.2021.104351

Negrini, M., Stunitz, H., Berger, A., Morales, L.F.G., 2014. The effect of deformation on the TitaniQ geothermobarometer: An experimental study. Contributions to Mineralogy and Petrology 167. https://doi.org/10.1007/s00410-014-0982-x

Okudaira, T., Jeřábek, P., Stünitz, H., Fusseis, F., 2015. High-temperature fracturing and subsequent grain-size-sensitive creep in lower crustal gabbros: Evidence for coseismic loading followed by creep during decaying stress in the lower crust. Journal of Geophysical Research: Solid Earth 120. https://doi.org/10.1002/2014JB011708

Palazzin, G., Raimbourg, H., Stünitz, H., Heilbronner, R., Neufeld, K., Précigout, J., 2018. Evolution in H_2O contents during deformation of polycrystalline quartz: An experimental study. Journal of Structural Geology 114. https://doi.org/10.1016/j.jsg.2018.05.021

Paterson, M.S., 1986. The thermodynamics of water in quartz. Physics and Chemistry of Minerals 13. https://doi.org/10.1007/BF00308276

Paterson, M.S., 1989. The interaction of water with quartz and its influence in dislocation flow: an overview. Rheology of Solids and of the Earth. New York: Oxford, 107–142.

Paterson, M.S., 2013. Materials Science for Structural Geology. Springer, Dordrecht. https://doi.org/https://doi.org/10.1007/978-94-007-5545-1

Paterson, M.S., Luan, F.C., 1990. Quartzite rheology under geological conditions. Geological Society Special Publication 54. https://doi.org/10.1144/GSL.SP.1990.054.01.26

Pec, M., 2014. Experimental investigation on the rheology of fault rocks. PhD thesis. Basel Universität.

Pec, M., Stünitz, H., Heilbronner, R., 2012. Semi-brittle deformation of granitoid gouges in shear experiments at elevated pressures and temperatures. Journal of Structural Geology 38. https://doi.org/10.1016/j.jsg.2011.09.001

Pec, M., Stünitz, H., Heilbronner, R., Drury, M., 2016. Semi-brittle flow of granitoid fault rocks in experiments. Journal of Geophysical Research: Solid Earth 121. https://doi.org/10.1002/2015JB012513

Pevik, J.A., 2015. Geological and mineralogical characterization of the upper part of the Gamasfjell Quartzite at the Vaggecearu Mountain. MSc thesis. NTNU Trondheim, p. 132.

Poirier, J.-P., Guillopé, M., 1979. Deformation induced recrystallization of minerals. Bulletin de Minéralogie 102, 67–74. https://doi.org/10.3406/bulmi.1979.7256

Précigout, J., Stünitz, H., 2016. Evidence of phase nucleation during olivine diffusion creep: A new perspective for mantle strain localisation. Earth and Planetary Science Letters 455. https://doi.org/10.1016/j.epsl.2016.09.029

Raimbourg, H., Vacelet, M., Ramboz, C., Famin, V., Augier, R., Palazzin, G., Yamaguchi, A., Kimura, G., 2015. Fluid circulation in the depths of accretionary prisms: An example of the Shimanto Belt, Kyushu, Japan. Tectonophysics 655. https://doi.org/10.1016/j.tecto.2015.05.023

Ramseyer, K., Baumann, J., Matter, A., Mullis, J., 1988. Cathodoluminescence Colours of α -Quartz . Mineralogical Magazine 52. https://doi.org/10.1180/minmag.1988.052.368.11

Renner, J., 1996. Experimentelle Untersuchungen zur Rheologie von Coesit. PhD thesis. Ruhr-Universität, Bochum.

Richter, B., Stünitz, H., Heilbronner, R., 2016. Stresses and pressures at the quartz-to-coesite phase transformation in shear deformation experiments. Journal of Geophysical Research: Solid Earth 121. https://doi.org/10.1002/2016JB013084

Richter, B., Stünitz, H., Heilbronner, R., 2018. The brittle-to-viscous transition in polycrystalline quartz: An experimental study. Journal of Structural Geology 114. https://doi.org/10.1016/j.jsg.2018.06.005

Rovetta, M.R., Holloway, J.R., Blacic, J.D., 1986. Solubility of hydroxyl in natural quartz annealed in water at 900°C and 1.5 GPa. Geophysical Research Letters 13. https://doi.org/10.1029/GL013i002p00145

Rusk, B.G., Lowers, H.A., Reed, M.H., 2008. Trace elements in hydrothermal quartz: Relationships to cathodoluminescent textures and insights into vein formation. Geology 36. https://doi.org/10.1130/G24580A.1

Rutter, E.H., Brodie, K.H., 2004a. Experimental intracrystalline plastic flow in hot-pressed synthetic quartzite prepared from Brazilian quartz crystals. Journal of Structural Geology 26. https://doi.org/10.1016/S0191-8141(03)00096-8

Rutter, E.H., Brodie, K.H., 2004b. Experimental grain size-sensitive flow of hot-pressed Brazilian quartz aggregates. Journal of Structural Geology 26. https://doi.org/10.1016/j.jsg.2004.04.006

Rutter, E.H., Neumann, D.H.K., 1995. Experimental deformation of partially molten Westerly granite under fluid-absent conditions, with implications for the extraction of granitic magmas. Journal of Geophysical Research 100. https://doi.org/10.1029/94jb03388

Schmid, S., Casey, M., 1986. Complete fabric analysis of some commonly observed quartz c-axis patterns. Geophysical Monograph 36, 263–286.

Schmocker, M., Bystricky, M., Kunze, K., Burlini, L., Stünitz, H., Burg, J.-P., 2003. Granular flow and Riedel band formation in water-rich quartz aggregates experimentally deformed in torsion. Journal of Geophysical Research: Solid Earth 108. https://doi.org/10.1029/2002jb001958

Spear, F.S., Wark, D.A., 2009. Cathodoluminescence imaging and titanium thermometry in metamorphic quartz. Journal of Metamorphic Geology 27. https://doi.org/10.1111/j.1525-1314.2009.00813.x

Stipp, M., Kunze, K., 2008. Dynamic recrystallization near the brittle-plastic transition in naturally and experimentally deformed quartz aggregates. Tectonophysics 448. https://doi.org/10.1016/j.tecto.2007.11.041

Stipp, M., Stünitz, H., Heilbronner, R., Schmid, S.M., 2002a. Dynamic recrystallization of quartz: Correlation between natural and experimental conditions. Geological Society Special Publication 200, 171–190. https://doi.org/10.1144/GSL.SP.2001.200.01.11

Stipp, M., Stünitz, H., Heilbronner, R., Schmid, S.M., 2002b. The eastern Tonale fault zone: A “natural laboratory” for crystal plastic deformation of quartz over a temperature range from 250 to 700 °C. Journal of Structural Geology 24. https://doi.org/10.1016/S0191-8141(02)00035-4

Stipp, M., Tullis, J., 2003. The recrystallized grain size piezometer for quartz. Geophysical Research Letters 30. https://doi.org/10.1029/2003GL018444

Stipp, M., Tullis, J., Behrens, H., 2006. Effect of water on the dislocation creep microstructure and flow stress of quartz and implications for the recrystallized grain size piezometer. Journal of Geophysical Research: Solid Earth 111. https://doi.org/10.1029/2005JB003852

Størseth, L.R., Wanwik, J.E., 1992. Kvartsressurser i Finnmark.

Stünitz, H., 1998. Syndeformational recrystallization - Dynamic or compositionally induced? Contributions to Mineralogy and Petrology 131. https://doi.org/10.1007/s004100050390

Stünitz, H., Fitz Gerald, J.D., 1993. Deformation of granitoids at low metamorphic grade. II: Granular flow in albite-rich mylonites. Tectonophysics 221. https://doi.org/10.1016/0040-1951(93)90164-F

Stünitz, H., Fitz Gerald, J.D., Tullis, J., 2003. Dislocation generation, slip systems, and dynamic recrystallization in experimentally deformed plagioclase single crystals. Tectonophysics 372. https://doi.org/10.1016/S0040-1951(03)00241-5

Stünitz, H., Thust, A., Heilbronner, R., Behrens, H., Kilian, R., Tarantola, A., Fitz Gerald, J.D., 2017. Water redistribution in experimentally deformed natural milky quartz single crystals—Implications for H_2O-weakening processes. Journal of Geophysical Research: Solid Earth 122, 866–894. https://doi.org/10.1002/2016JB013533

Tarantola, A., Diamond, L.W., Stünitz, H., 2010. Modification of fluid inclusions in quartz by deviatoric stress I: Experimentally induced changes in inclusion shapes and microstructures. Contributions to Mineralogy and Petrology 160. https://doi.org/10.1007/s00410-010-0509-z

Tokle, L., Hirth, G., Behr, W.M., 2019. Flow laws and fabric transitions in wet quartzite. Earth and Planetary Science Letters 505, 152–161. https://doi.org/10.1016/j.epsl.2018.10.017

Trepmann, C.A., Stöckhert, B., 2013. Short-wavelength undulatory extinction in quartz recording coseismic deformation in the middle crust – An experimental study. Solid Earth 4, 263–276. https://doi.org/10.5194/se-4-263-2013

Trepmann, C.A., Stöckhert, B., 2003. Quartz microstructures developed during non-steady state plastic flowat rapidly decaying stress and strain rate. Journal of Structural Geology 25. https://doi.org/10.1016/S0191-8141(03)00073-7

Trepmann, C.A., Stöckhert, B., Dorner, D., Moghadam, R.H., Küster, M., Röller, K., 2007. Simulating coseismic deformation of quartz in the middle crust and fabric evolution during postseismic stress relaxation - An experimental study. Tectonophysics 442. https://doi.org/10.1016/j.tecto.2007.05.005

Tullis, T.E., Tullis, J., 1986. Experimental rock deformation techniques. Mineral and Rock Deformation: Laboratory Studies. American Geophysical Union, Washington, DC, 297–324. https://doi.org/10.1029/gm036p0297

Underwood, E.E., 1968. Particle-size distribution. Quantitative Microscopy. 149–200.

Urai, J.L., Means, W.D., Lister, G.S., 1986. Dynamic recrystallization of minerals. Mineral and Rock Deformation: Laboratory Studies. AGU, Washington, DC, 161–199.

Van Daalen, M., Heilbronner, R., Kunze, K., 1999. Orientation analysis of localized shear deformation in quartz fibres at the brittle-ductile transition. Tectonophysics 303. https://doi.org/10.1016/S0040-1951(98)00264-9

Vernooij, M.G.C., Kunze, K., den Brok, B., 2006. “Brittle” shear zones in experimentally deformed quartz single crystals. Journal of Structural Geology 28. https://doi.org/10.1016/j.jsg.2006.03.018

APPENDICES

Appendix 1. Schematic description of sample assembly, as placed in the pressure vessel.

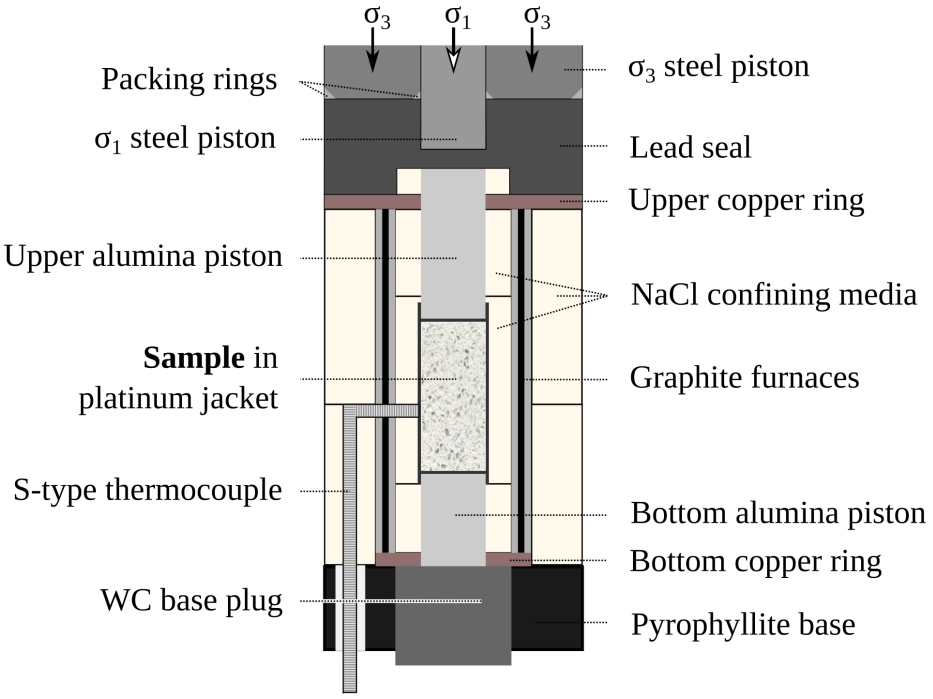

Appendix 2. Example of the mechanical record of a constant conditions experiment (sample 547PP; see Table 1 for full experimental conditions). The σ_1 stress is shown by the red line, confining pressure by the green line and displacement of the σ_1 piston by the blue line. **a)** The entire duration of the experiment divided into 6 stages; **b)** zoom to the pumping-up stage 1, with temperature increment steps marked at the stress curve; **c)** zoom to the hit-point evaluation at stage 4; **d)** zoom to the quenching part at stage 6.

Slow and progressive increase of pressure and temperature up to desired starting conditions (stage 1) was managed by advancing both external σ_1 and σ_3 pistons and controlling the direct current flow through the highly resistant graphite furnace. The σ_1 piston was run by a mechanical gear system, while advancement of the σ_3 piston was controlled by a hydraulic pumping system. When the desired starting conditions were reached, the sample assembly was kept at the hot-pressing stage for ~12 hours before the onset of deformation (stage 2). The experiment started by advancing the σ_1 piston through the top lead seal, in order to get into direct contact with the upper alumina forcing block in the assembly (see Renner (1996) for more details). Once the load applied to the σ_1 piston increased enough to plunge the piston into the lead seal, penetration through the seal was followed by slow and gradual stress increase identified as the run-in stage of the stress record curve (stage 3). At the end of the run-in stage, as the steel piston was getting in direct contact with the alumina forcing block, the stress started to increase sharply, defining the loading stage of the stress curve. Intersection of tangent lines of the run-in and loading stages of the stress curve defined a hit-point (stage 4) indicating an onset of deformation. After the yield stress has been reached, the samples were deforming at either constant, increasing, or decreasing stress (stage 5). When the desired strain was achieved, the experiments had been quenched down to 200 °C within 2-3 min, followed by a slow σ_1 piston retreat, keeping the stress slightly greater than the confining pressure. The samples were gradually depressurized and cooled down to the room temperature within 2 hours (stage 6). The full experimental procedure is described in more detail in Richter et al. (2016).

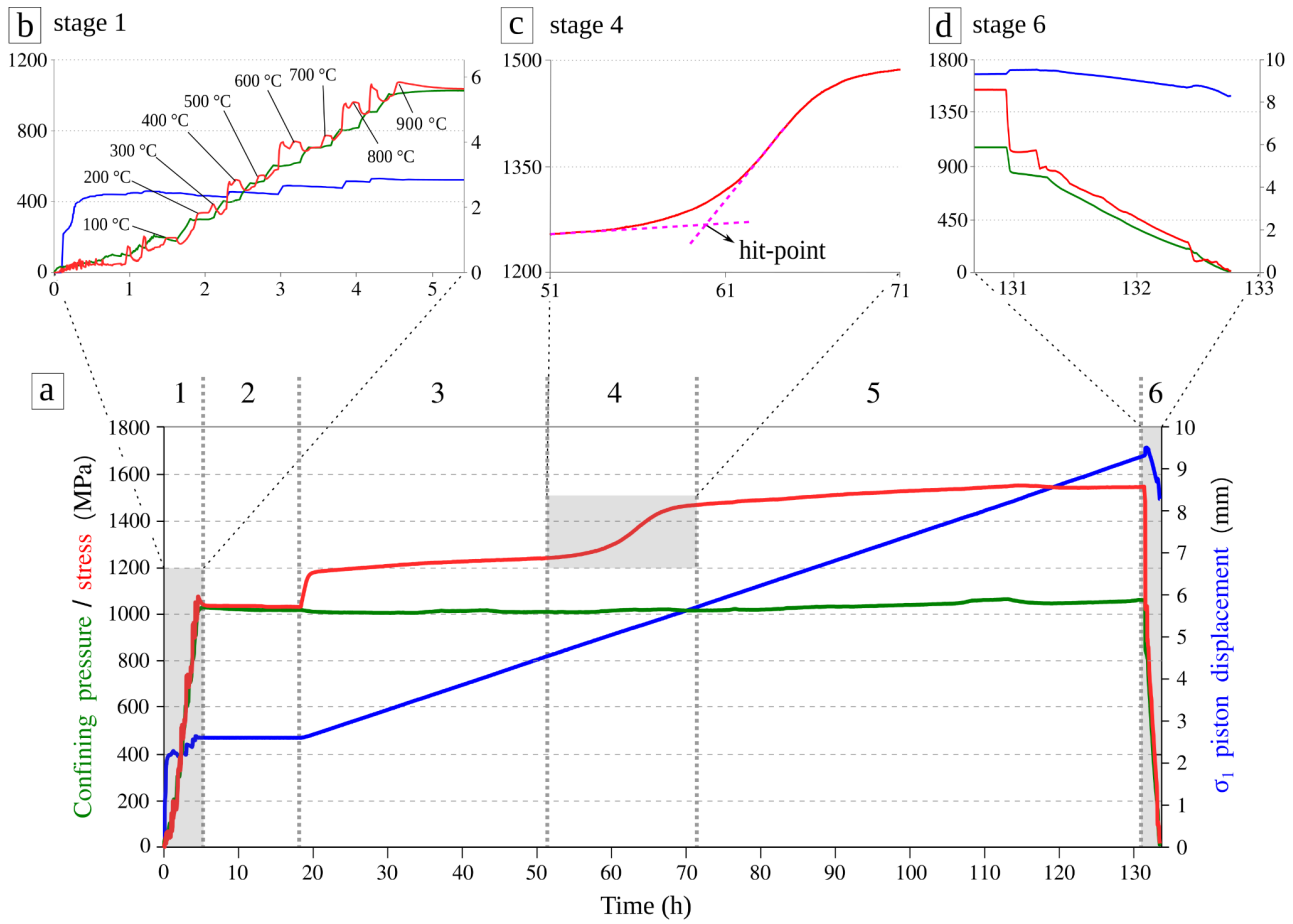

Appendix 3. CL colors explained by combination of luminescence emission bands at particular wavelengths. Colors of the spectral lines correspond to the approximate color as visible in the CL maps. Original sand grains appear in shades of yellow, orange and cyan-blue, cement in brown and reconstituted material after deformation in blue.

Various emission bands are caused by specific types of defects in the quartz crystal lattice, some of which are caused by incorporation of trace elements (Ramseyer et al., 1988; Götze et al., 2001; Götze, 2012). All CL colors related to original grains result from pronounced emission bands around 650 nm wavelengths. The difference between the colors is controlled by intensity of the emission band around 450 nm. If the 450 nm band is negligible, the grain will be visible in yellow shades, while small intensities of the 450 nm band will change it to orange. As the intensity of the 450 nm band is increasing, the CL color of a grain will turn to cyan-blue. Brown CL color of the cement typically shows the same major emission band as for the grains (650 nm), but with much lower intensities.

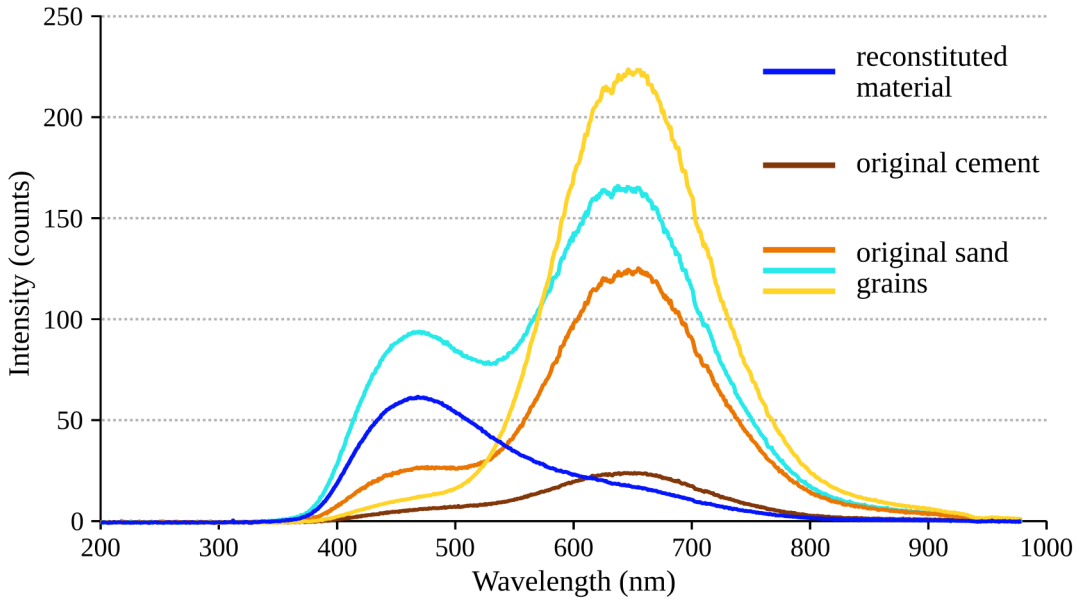

Appendix 4. Microstructure of a hot-pressed as-is sample 592PP, in **(a)** cross polarized light and **(b)** CL image, confirming absence of the lateral mode I cracks parallel to σ_1 direction at this stage of experiment.

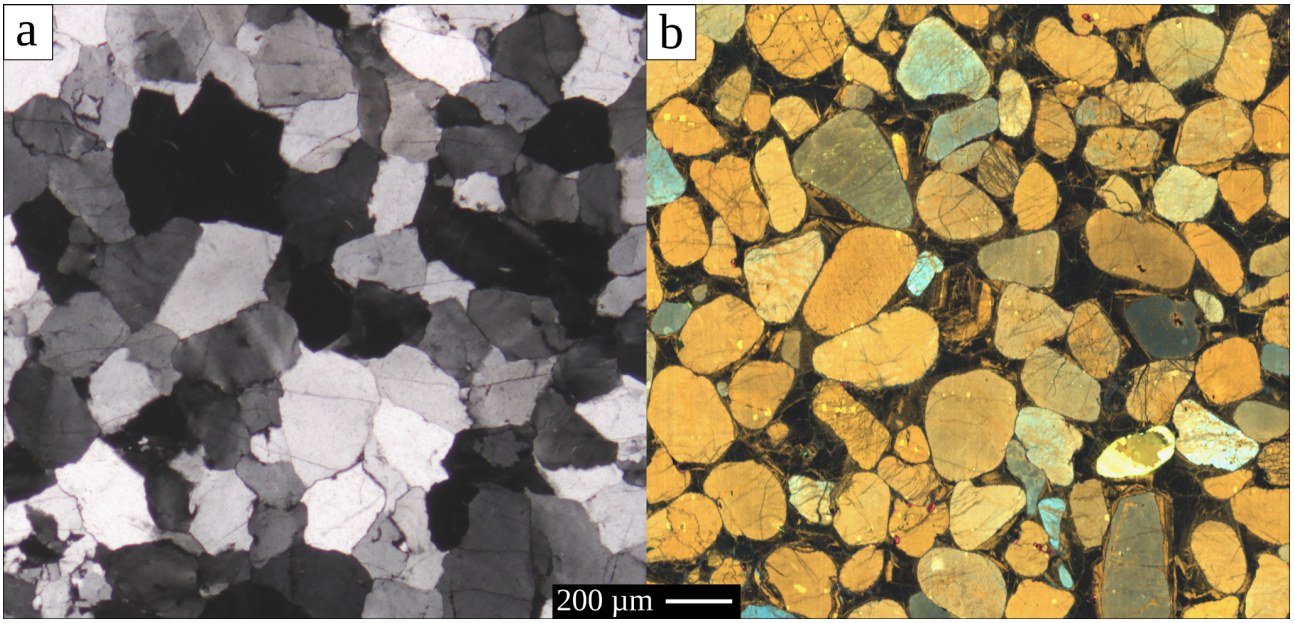

Appendix 5. Detailed description of misorientation relationship reflected by internal plasticity

The LCD domains generally show a good match in positions of misorientation axes in inverse pole figures for the original and recrystallized grains. The small portions of original grains G2 and G3 adjacent to the LCD domain in the as-is sample 568PP (**Fig. 10a**) show maxima of misorientation axes close to m-axis and partly also c-axis, similar to the whole grains G2 and G3 (cf. **Fig. 10c** and **e**). The HAGB contact of the LCD recrystallized domain with G3 shows misorientation axes in similar position as for the LAIBs and LASBs in G3, while the contact with G2 shows position of misorientation axes close to the z-rhomb axis. This observation is compatible with the recrystallized grains showing orientation relation to G3 and not to G2 (LCD in **Fig. 10d**), as well as with location of the misorientation axis between G2 and G3 near the z-rhomb axis (pink dots in inverse pole figures in **Fig. 10e**). Therefore, the contact between the recrystallized domain and G2 (**Fig. 10e**) most likely corresponds to the original boundary between the G2 and G3 grains. The LASBs and HAGBs misorientation axes within the LCD recrystallization domain show maxima close to c-axis orientation, with fewer misorientation axes close to the m-axis. The LCD-2 domain between G1 and G5 and LCD-4 between G6 and G7 in the H_2O-added sample 567PP (**Fig. 11c**) show a similar position of misorientation axes within the original grains, across the contacts between the original grains and recrystallized domains, as well as within the recrystallized domains (**Fig. 12d**). Assuming the tilt boundaries only, the positions of the misorientation axes in the LCD domains can be related to activation of {m}<a>, {z}<a> and {c}<a> slip systems (see **Fig. 10b**).

The HCD domains show relatively poor correlation in the distribution of misorientation axes for the original and the recrystallized grains (**Figs. 10e** and **12e**). The HCD domain in the as-is sample 568PP (**Fig. 10a**) shows maxima of misorientation axes in G2 close to m-axis and in G3 close to c-axis, while their contact with the recrystallized domain and the LASBs and HAGBs in the recrystallized domain show maxima of misorientation axes close to z-rhomb (**Fig. 10e**). The contact between the recrystallized domain and G3 shows a misorientation maximum matching the misorientation between G2 and G3 (pink dots in inverse pole figures in **Fig. 10e**). This observation is compatible with the orientation relation of recrystallized grains to G2 and not to G3 (HCD in **Fig. 10d**), suggesting that the contact between the recrystallized domain and G3 represents the original boundary between G2 and G3 grains. The HCD-1 domain in the H_2O-added sample 567PP (**Fig. 11c**) shows only a partial match in position of misorientation axes, close to a-axis, within G1 and across its contact with the recrystallized domain (**Fig. 12e**). The other contact shows no match in position of misorientation axes within G3 and its contact with the recrystallized domain. The recrystallized domain shows misorientation axes across the LASBs and HAGBs located close to the c-axis and m-axis. Although the misorientation axes within the HCD domains can be associated with dislocation creep and activation of {m}<a>, {z}<a> and {c}<a> slip systems (see **Fig. 10b**), the lack of clear misorientation relations across the contacts with the original grains suggests that the HCD domains originated from cracking and local fragmentation of the original grains.